Controlling Metal Organic Framework (MOF) Crystallization Using High Throughput Synthesis and Computer Vision

Qusai Abdulkhaliq Alsabia

A thesis
submitted in partial fulfillment of the
requirements for the degree of

Master of Science

University of Washington

2025

Committee:

Shijing Sun

Dianne Xiao

Program Authorized to Offer Degree:

Chemistry

University of Washington

Abstract

Controlling Metal Organic Framework (MOF) Crystallization Using High Throughput Synthesis and Computer Vision

Qusai Abdulkhaliq Alsabia

Chair of Supervisory Committee:

Shijing Sun

Department of Chemistry

Co_2(dobdc) is a metal organic framework (MOF) that is essentially used in gas separation. Problems with current synthetic solvothermal routes involve a lack of creativity, the obtaining of elongated needle-shaped crystals along the c-axis with a high aspect ratio (AR), and slow synthetic approaches. Herein, we propose automating the synthesis of Co_2(dobdc) MOFs using the OT-2 liquid handling robot (*Mara*) to improve experimental design for higher throughput, improved accuracy and increased efficiency. By doing so, we introduce strategies to create Co_2(dobdc) MOFs with lower ARs in accelerated high throughput manner and characterize crystals with novel computer vision algorithm, *Bok Choy*. AR is a unit-less measurement for the fraction of the width by length of a crystal. Lower ARs are significantly important for MOFs to grant more control over porosity, augment surface-to-volume ratio, and enhance the characteristics of MOFs such as colloidal dispersion, diffusion, catalysis, mechanical strength, and anisotropic properties. With these strategies, we solve a set of drawbacks in synthesizing MOFs in lab such as low throughput, safety risks, human error and time consumption

Dedication

To my mother, father, family, friends and mentors.
Your unconditional support and faith in me
have been great factors in this journey. Thank you.

Acknowledgments

For all of the knowledge and skills that I have gained throughout this project, I would like to acknowledge the people who contributed to my success especially:

Saudi Arabian Ministry of Education

Dr. Shijing Sun

Dr. Dianne Xiao

Dr. Brandi Cossairt

Douglas Baumgardner, PhD Student

Dr. Samantha Young

Dr. Ellen Lavoie

Dr. Dan Graham

Arthur Chong, RA

Andrew McDaniel, PhD Student

Clara Tamura, PhD Student

Hemanth N. Ramesh

NanoEIS

Introduction

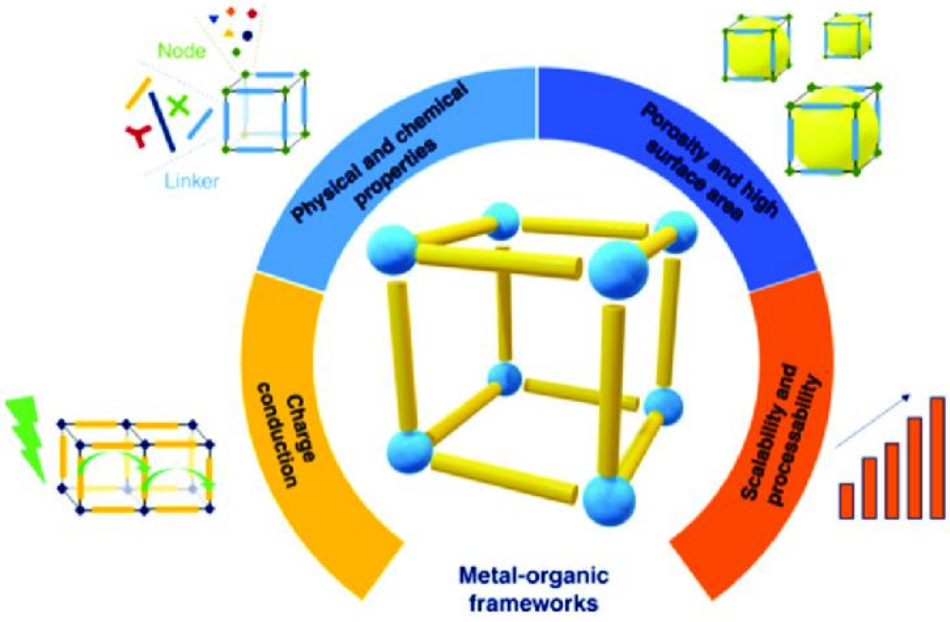

Figure 1 shows a schematic of MOFs with metal nodes (blue) connected by organic linkers (yellow) surrounded by some important features of MOFs.

MOFs are a class of porous materials comprised of metal nodes structured with organic linkers. Such a coordination endows MOFs with a blend of extraordinary properties such as high porosity, large surface area, and tunable physical and chemical characteristics, making them highly versatile for various applications (Dutt, 2023). MOFs can be tailored to achieve specific functionalities, offering significant prospective in fields such as catalysis, gas storage, and separation technologies.

A typical schematic of MOFs (Figure 1) highlights their structural components—metal nodes and organic linkers—and highlights fundamental features, such as charge conduction, scalability, and processability, which illustrate MOFs as exceptionally valuable in engineering cutting-edge materials for industrial means.

Optimizing the synthesis of MOFs, therefore, has been one of the most important missions in material science and engineering particularly due to the challenges and difficulties associated with it. With limitations present in a MOFs sample, their full potential would be incomplete and obstructed.

Present challenges in MOFs synthetic approaches involve difficulties in yielding MOFs with low ARs as the intricacy of crystallization under different reaction parameters often produce inconsistent outcomes. Furthermore, the lack of innovation in MOF synthesis is an obstacle in material science as existing production methods are controlled by conventional methods that constraint innovation and efficiency. The dependence on manual methods impedes discovering creatively designed synthetic tools. Moreover, challenges in enhancing MOFs synthesis are

associated with the steps in creating MOFs that require vigilant tuning of reaction conditions, precursors, and parameters.

In this paper, we attempt to generate a set of standardized, high-throughput procedures to accelerate attaining highly reproducible and scalable MOFs. This is doable by concentrating on finding the solutions for such challenges by leveraging a high-throughput automated synthesis as a transformative tactic to quicken the optimization of MOFs properties. By integrating advanced tools such as the *Mara* liquid handler, which enables accurate, automated conduct of chemicals under measured conditions following stress-free calibration. This handler is smart to communicate and operate with desired software, mainly Opentrons API and Python to accommodatingly deliver effortlessly adjustable automation to simplify and tailor experimental workflows. Eventually rendering automation of Co_2(dobdc) synthesis as refined and originative solution as possible that constantly improve both quality and acceleration of the method.

The AR of MOFs is essentially responsible for determining MOFs performance in their designed applications. Lower ARs are characterized by less elongated and likely uniform crystal shapes, offering numerous gains that straightforwardly boost the functionality of MOFs. These benefits, as outlined by Wang et al. include enhanced diffusion, increased surface area, improved scattering in solutions, uniformity of crystal shape, and decreased path lengths, which collectively improve gas adsorption, catalysis, scalability, and reproducibility (2024). For instance, efficiency and speed of reaction is guaranteed with decreased path length, and more active sites are accessible with higher surface area while uniformity is associated often with prevention of agglomeration (Wang et al., 2024).

To further discover the effect of MOFs features on hands-on applications, this study builds upon the findings of Colwell et al. (2021). Colwell et al.'s work inspected the synthesis of MOFs with varying ARs by means of differing the linkers as shown in Figure 2 and tested how changing Ars can interfere with efficiency on modern applications such as zero-column chromatography (ZCC).

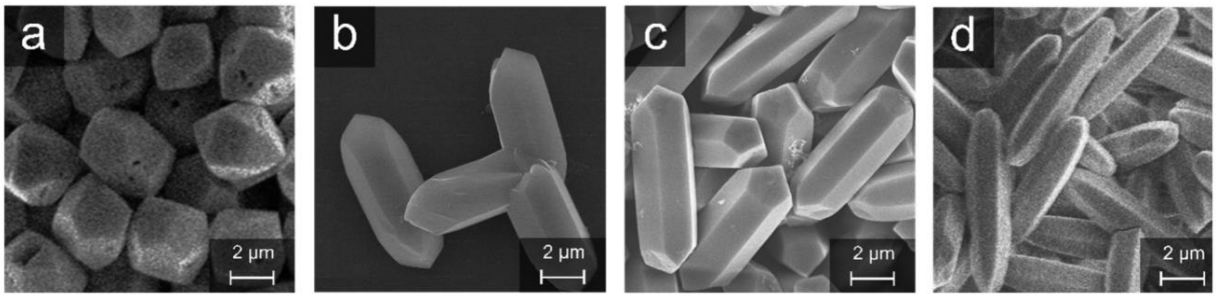

Figure 2 shows four different crystals of Co_2(dobdc) with different linkers: acetate, formate, chloroacetate, and trichloroacetate, respectively.

From Figure 2, different carboxylate metal salts were used in the synthesis method, leading to disparities in morphologies, especially in their ARs. While all examples showed uniformly shaped crystals separately, using acetate produced cube-like crystals, while using both formate and chloroacetate produced rod-like crystals with higher and similar ARs, and using trichloroacetate produced longer crystals with higher ARs (Colwell et al., 2021).

In this synthesis, H4dobdc and cobalt (II) acetate were mixed in a 1:1 water/ethanol and heated in a single crystal solvothermal route which gives crystals with a diamond-like figure called pentagonal dodecahedra (Colwell et al., 2021). Adding DMF to the mixture seems to have created rod-like crystals. While using formate instead of acetate as linker also leads to synthesizing low dispersity polyhedra with clearly defined facets (Colwell et al., 2021). That is, to achieve a lower AR and less extending crystallites, using cobalt (II) acetate appeared to be a better option than cobalt (II) formate (Colwell et al., 2021). However, it was a huge burden to reproduce these crystals with acetate linkers in our investigation.

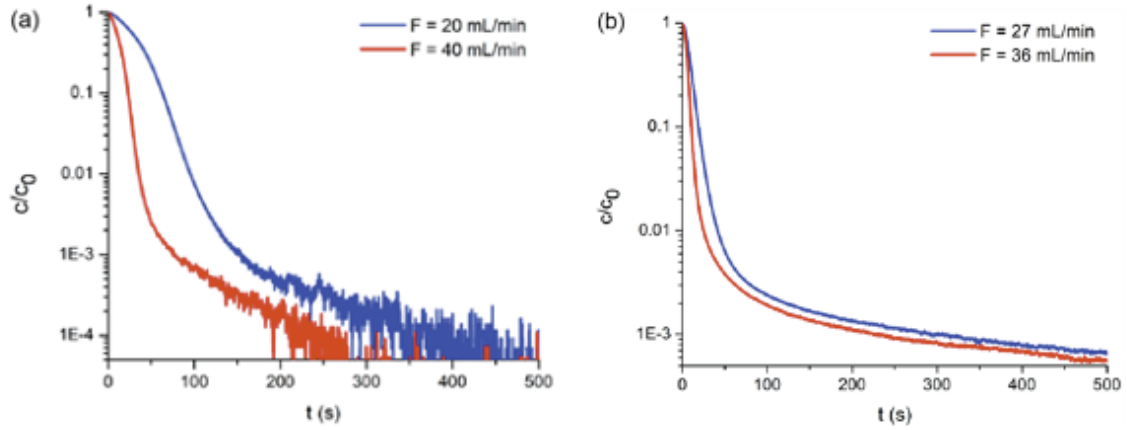

Figure 3 shows the recorded C/C_0 over time in seconds when long Ars crystals (left) and short Ars crystals (right) were used in m-xylene ZCC.

In Figure 3, ZCC was used to measure differences in the diffusion of m-xylene in the lowest and highest ARs of Co_2(dobdc) crystals from Figure 2. The C/C_0 describes the ratio of the final to the initial concentration of m-xylene and letter F on the top right describes the flow rate in mL/min. When long ARs crystals were used in the column, a linear plot with increasingly high noise levels was observed. Conversely, a logarithmic figure was generated when short ARs were used. Red colored lines indicate the purging or adding extra force to ease flow, while blue colored ones designate no external work. Differences in ARs were hypothesized to influence the functioning of MOFs in flow-through applications such as ZCC and were subsequently quantified to be congruent with initial expectations (Colwell et al., 2021).

Nonclassical Crystallization Pathways in MOFs

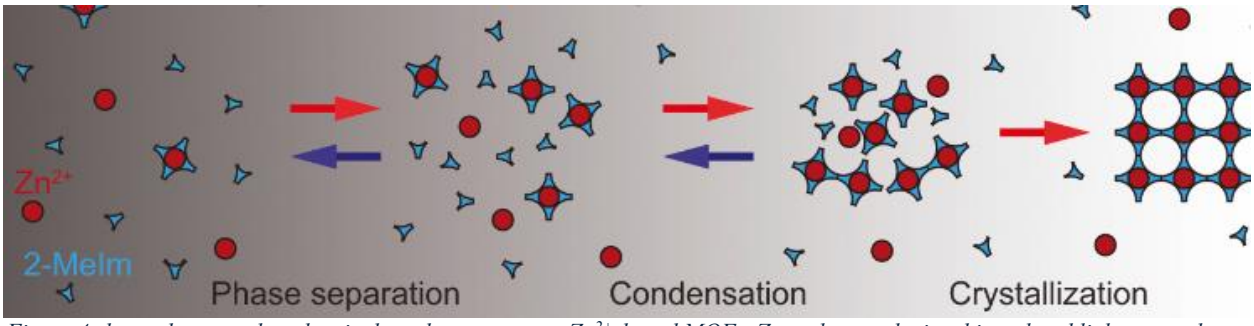

Figure 4 shows the steps that chemicals undergo to create Zn^{2+}-based MOFs. Zn nodes are depicted in red and linkers are shown in blue.

MOFs demonstrate a distinctive, nonclassical pathway for crystallization, as illustrated by Zn^{2+}-based MOFs. Contrasting classical crystallization, which progress through the direct nucleation and growth of a solid phase, MOF growth comprises intermediary phases that contain phase separation, such as liquid-liquid phases, and condensation of precursors before ultimate crystallization (Liu et al., 2021) and (Raptopoulou et al., 2021).

Following deprotonation of initial reagents in the presence of water and other solvents, the separation of metal ions (e.g., Zn^{2+}) and organic linkers (e.g., 2-Melm) occurs. This first stage is determined by supersaturation that leads to the construction of distinct domains supplemented in metal-organic precursors. Within such domains, coordination exchanges happen as the metal-organic precursors condense forming oligomeric masses. These clusters strive to strengthen molecular interactions out of the bulk material. Ultimately, the clusters sort of become self-assembled and transform into an well-arranged, permeable scaffold, obtaining the distinguishing organization of MOFs. Temperature, solvent volumes, metal-linker ratios, and time are all essential in determining the quality of MOFs as they interfere with this crystallization process (Liu et al., 2021) and (Raptopoulou et al., 2021).

As depicted in Figure 4, this pathway focuses on the step-by-step evolution from diffused particles to the final crystalline assembly. This nonclassical mechanism offers a clear understanding of how MOFs manifest and chances to examine such steps by varying interfering factors with MOF crystallization for modifying their morphologies and enhancing linked properties such as AR, size and shape that affect essential applications such as catalysis, gas storage and separation (Liu et al., 2021) and (Raptopoulou et al., 2021).

Our MOF: Co_2(dobdc)

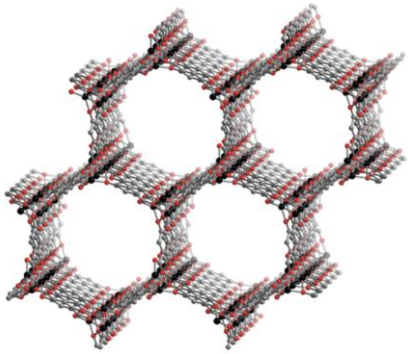

Figure 5 shows the porous hexagonal structure of M_2(dobdc) MOFs that extends along the c-axis.

The focus of this project is Co_2(dobdc), a member of the M_2(dobdc) series of MOFs, where M signifies divalent transition metal ions: Mg, Mn, Fe, Co, Ni, and Zn. These MOFs are characterized by Lewis acidic metal centers and Lewis basic organic linkers, offering a vigorous and resourceful structure for various applications. Co_2(dobdc) MOFs are endowed with a hexagonal overall shape comprised with a pact of metal cores harmonized to organic linkers, founding an extremely porous form. As shown in Figure 5, the crystalline structure of

Co_2(dobdc) reveals its c-axis extending, ordered geometry, which is a structural hallmark of the M_2(dobdc) series.

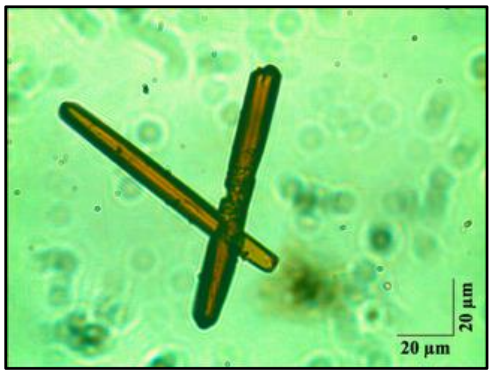

Figure 6 shows an initially synthesized Co_2(dobdc) crystal mounted on a glass slide and imaged with 50X upright microscope.

Furthermore, the microscopic inspection of one of the earliest synthesized Co_2(dobdc) crystals in this study (Figure 6) depicts their distinct extension along the c-xis. These rod-like crystals reflect the obstacle in controlling these MOFs ARs during the synthesis, which is a a burden that goes against their functional performance. The hexagonal images were reported and obtained from articles published by Sumida et al. (2012), which surveyed the structural aspects of Co_2(dobdc). This investigation further progresses the understanding of Co_2(dobdc) by exploring the relationship between ARs and the initial reaction conditions that lead to the lowest ARs.

Goals of the Project

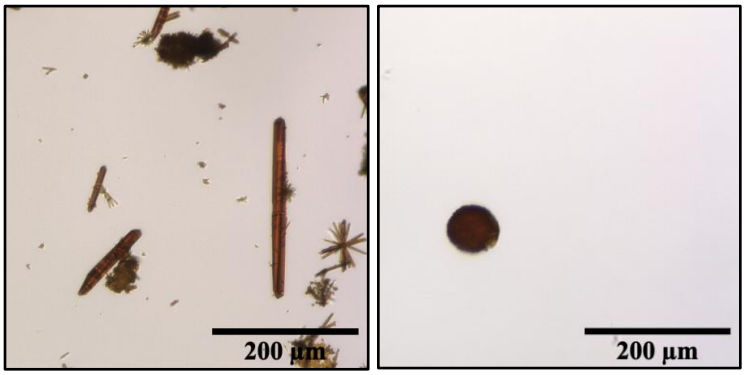

Figure 7 shows the baseline vs. the optimally obtained ARs in this investigation.

By concentrating on the use of automated synthesis of MOFs with computer vision to characterize MOFs with desirable ARs, this research seeks to identify first synthesize MOFs with the lowest ARs possible while obtaining uniformly shaped crystals. Second, we strive to identify the specific synthetic conditions that give these ARs. Also, we seek to quantify how ARs vary across distinctive synthetic conditions, specifying an inclusive comprehending of the connection between reaction parameters and crystal assets. By methodically assessing these aspects, this investigation contributes to enhancing the scalability of MOF synthesis for tailored applications. Figure 7 shows an example of baseline crystals with the highest AR and an example of crystals with the lowest AR achieved.

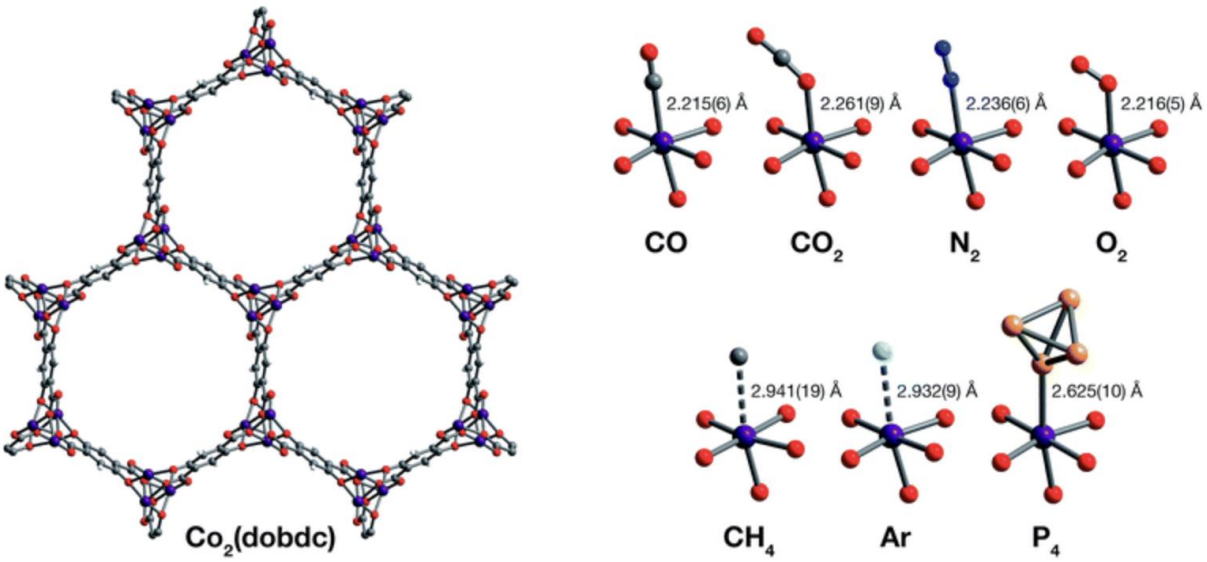

Figure 8 shows Co2dobdc structure (left) and examples of single interaction of metal Co nodes (purple) and various gases along with the distance between Co and mentioned gases in Angstroms.

Co_2(dobdc) is known for its unique stability and property of interacting with numerous guest molecules due to the easily accessible Co active sites due to the high porosity. One measurable quantity is the Co-X gas distances (Figure 8), where X represents the gas being hosted. This distance is measured in Angstroms and reported to assess the molecular interactions between the active sites and the gas molecule with a high degree of accuracy (Gonzales et al., 2017). Another measurable quantity that is particularly useful in these MOFs is called the occupancy of guest molecules at the cobalt (II) sites, which is the percentage of adsorption calculated as a fractional occupancy of one unit of guest particles assigned at one Co^{2+} active site. (Gonzales et al., 2017). These cobalt cores, while unstable in separation, are stabilized within the MOF as they allow for guest molecule binding (Figure 9).

Calculating differential enthalpies helps with essential thermodynamic insights into guest-framework communications, which is easily performed due to Co_2(dobdc) porous structure. Remarkably, Co_2(dobdc) was the first MOF where exchanges between CH_4 and a metal, as well as Ar and a metal, were observed and quantified (Gonzales et al., 2017).

Co_2(dobdc) has been reported to be an essential MOF exploited for capturing CO_2 competently, signifying its value in environmentally friendly technologies. Beyond CO_2, Co_2(dobdc) can be a bright candidate for the arrest of other gases, such as hydrogen (H_2), due to its flexible porosity and strong affinity. The structural adaptability of Co_2(dobdc), as illustrated in Figure 8, highlights the importance in advancing MOF-based technologies. Building upon the foundational work of Gonzalez et al. (2017), this research seeks to explore the synthesis and application of Co_2(dobdc) in greater depth, with a focus on optimizing its performance for targeted gas capture and separation processes.

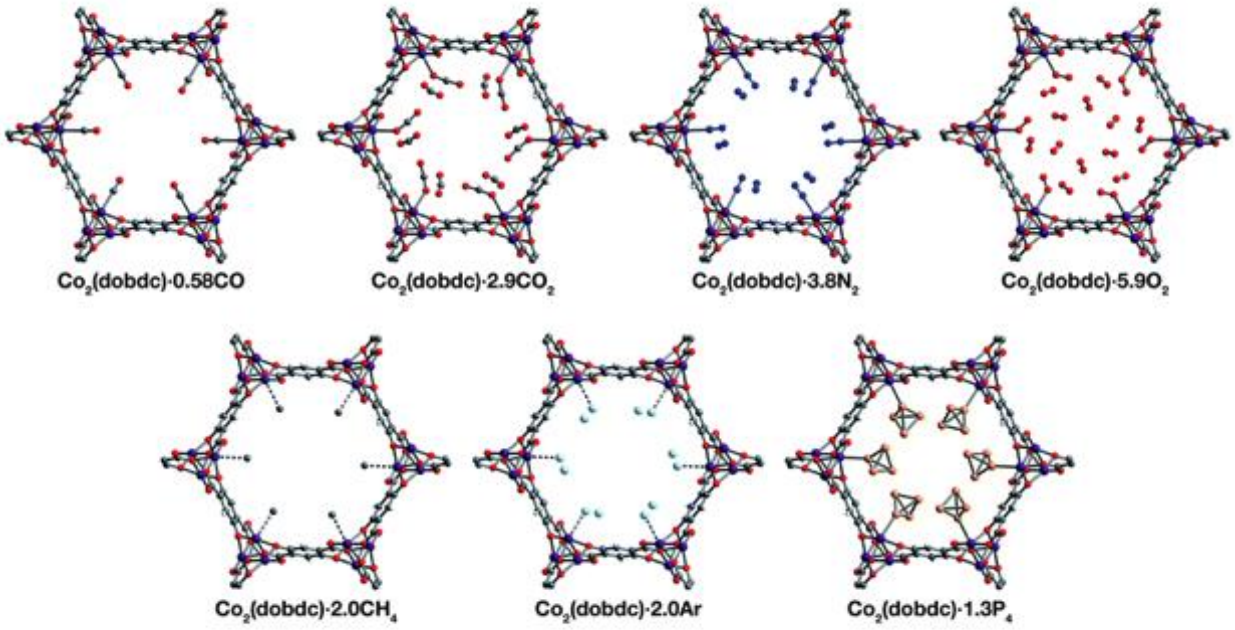

Figure 9 shows how the Co2(dobdc) MOF interact with different gases based on orientation and occupancy as well as applied pressures.

For gaining a deeper comprehension of the bonding between the MOF and several gaseous molecules, Gonzalez et al. performed a special *in-situ* X-ray diffraction experiment with an exceptional analytical tool that paves the way to analyze single crystals (2017). Eventually, they tested metal-gas adsorption processes under different pressures and temperatures, linking how molecules have different tendencies of forming bonds on active sites in terms of occupancy (2017). According to Gonzalez et al.'s experiment (Figure 9), Co_2(dobdc) was found to be able to withstand a wide range of pressures and temperatures (up to 250 K) customized to fit with the properties of guest molecules making it a versatile and excellent candidate for cutting-edge gas capture applications (2017).

As illustrated in Figure 9, Co_2(dobdc) reveals the ability of this MOF to adsorb an assortment of gas molecules such as carbon monoxide (CO), carbon dioxide (CO_2), nitrogen (N_2), oxygen (O_2), methane (CH_4), argon (Ar), and phosphine (P_3). With single crystal analysis using *in-situ* X-ray diffraction (XRD), Gonzalez et al. could examine the exact positioning of gas molecules within the MOF and assess the strength of bonds and report the quantitative occupancies. For instance, Co_2(dobdc) binds to about 5.9 O_2 molecules per unit under defined conditions of temperature and pressure, validating its high storage capacity.

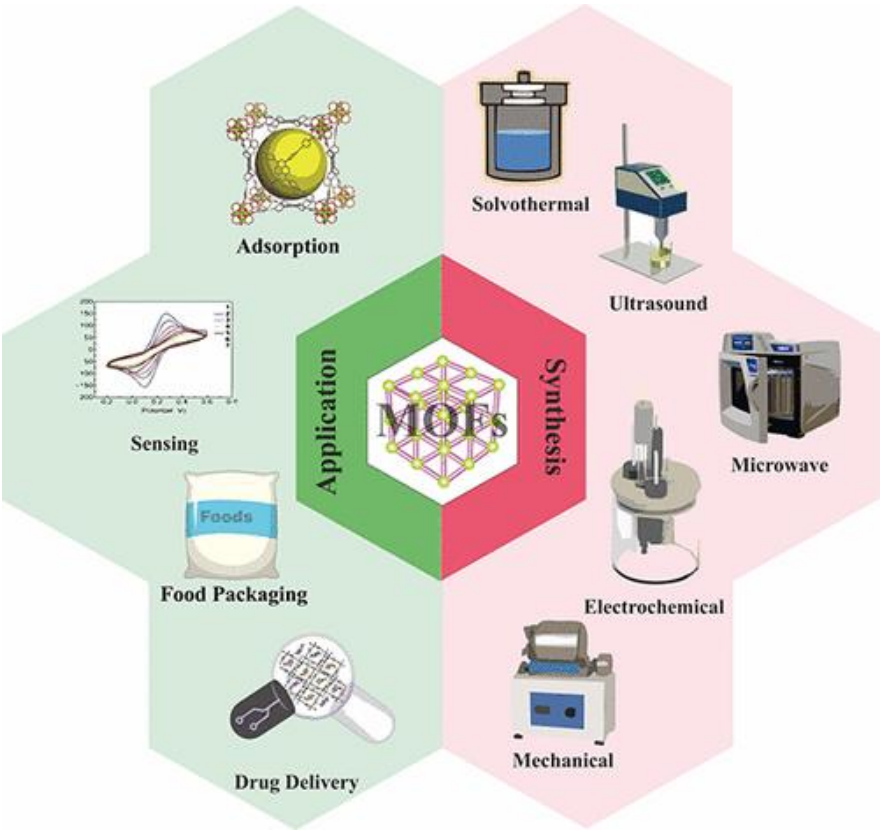

Figure 10 illustrates several means to synthesize MOFs (red) in contrast to several applications of MOFs (green).

There are several means that can be used to synthesize desirable MOFs, each endowed with advantages designed to obtain specific properties. The most common method is known as the solvothermal synthetic approach, which is briefly mixing solvents such as water and ethanol with metal and linker chemical sources in the form of solids that are eventually heated at specified temperature to prevent introducing multiple phases in the framework (Sani, 2024). For instance, heating a solution of mixtures at 100 C constantly for a set duration of time is supposed to produce one well-defined and easily characterized phase, whereas heating another solution while the temperature is rising from 0 to 100 C can yield multiple phases in the sample. This study uses this kind of synthesis.

Another approach is the ultrasound-assisted synthesis, which exploits ultrasonic waves to speed up chemical reactions. This approach reduces synthesis time while increasing surface area and homogeneity of the produced set of crystals. Comparably, the microwave-based method affords swift and even heating with electromagnetic radiation, drastically cutting reaction duration compared to established routine methods and expected to yield MOFs that are homogenous (Sani, 2024).

One notable strategy is the electrochemical synthesis, by which an electric current is exploited to initiate and propel the release of metal ions from an electrode in a solution filled with dissolved linkers, which is especially helpful for precise control over the MOF growth and easier scalability (Sani, 2024).

Methods

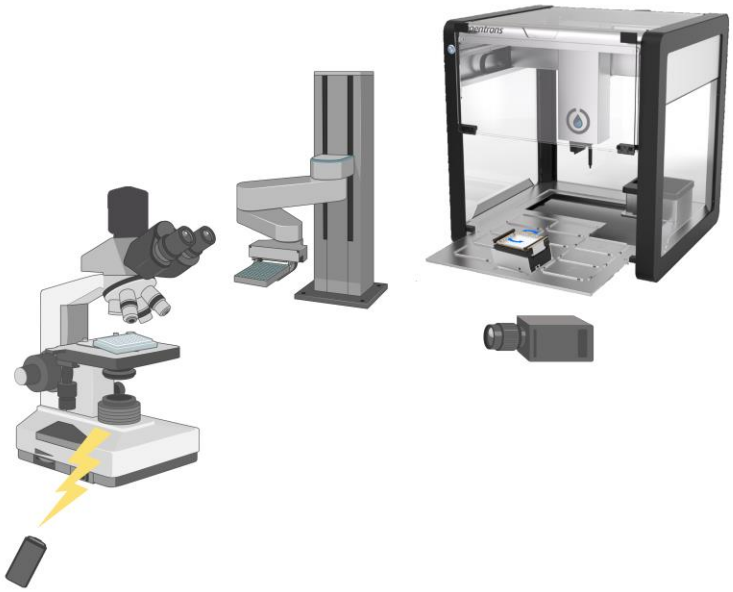

Figure 11 illustrates the liquid handling robot Mara (right), automated handler and transformer (center), and inverted microscope (left).

The characterization and synthesis of MOFs entail the integration of automated tools that accelerates obtaining consistent and reproducible results in a creative and novel manner. For this goal, this study builds a high-throughput system that pools optical microscopy, automated handling systems, and *Mara*.

Automating synthesis using *Mara* OT-2 Robot

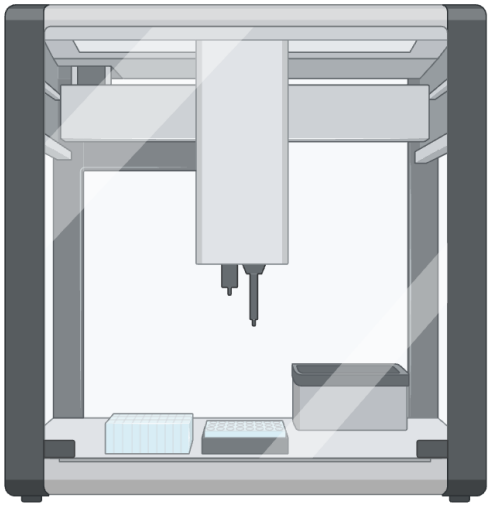

Figure 12 shows a BioRender image of the Mara robot.

Supported by Python and Opentrons API, *Mara* was used to understand the Python detailed commands to accelerate the synthesis of more than 40 samples per workday for the needs of this study as it can generate even more samples. In the commands, we were able to detail intricately defined quantities designed for each sample. In doing so, Mara was able to efficiently facilitate the mixing of reagents, agitating mixtures by pipetting and re-pipetting solutions, and heating with its equipped heater/shaker adapter. Therefore, we were able eliminate irregularities presented by human error and pointedly reduce the time required to actively administer the experiment.

Automating characterization using EVOS optical inverted microscope

Figure 13 shows a BioRender image of the EVOS microscope proivded by the UW MAF center.

Using EVOS automated microscope, the MOFs where imaged using high resolution 4X, 10X and 20X objectives with its integrated camera and automated stage, the system captures detailed visuals of crystal morphology, where crystallization was assessed in every sample. This special microscope was essentially helpful in its ability to find samples inside the wells of the well-plate automatically by finding the right focus with one click. Additionally, samples were easily examined by tapping a certain point of well-plate featured map that EVOS can arrive at and image with a simple click. Furthermore, it is endowed with several other features beyond the scope of this description. The images were saved using the UW Molecular Analysis Facility (MAF) center storage software. Hereafter, the images were named and organized in our excel document, which is available in the following link: https://docs.google.com/spreadsheets/d/1Yu8tQ21ecnXXWMwQ2opjShibP1-eaOzA5lmcHhQKQ1Q/edit?gid=1142696481#gid=1142696481. Lastly, the images were arranged into our database, which can be accessible using this link: https://github.com/uwsunlab/mof_dataset.

Automating image analysis using Python supported algorithm *Bok Choy*

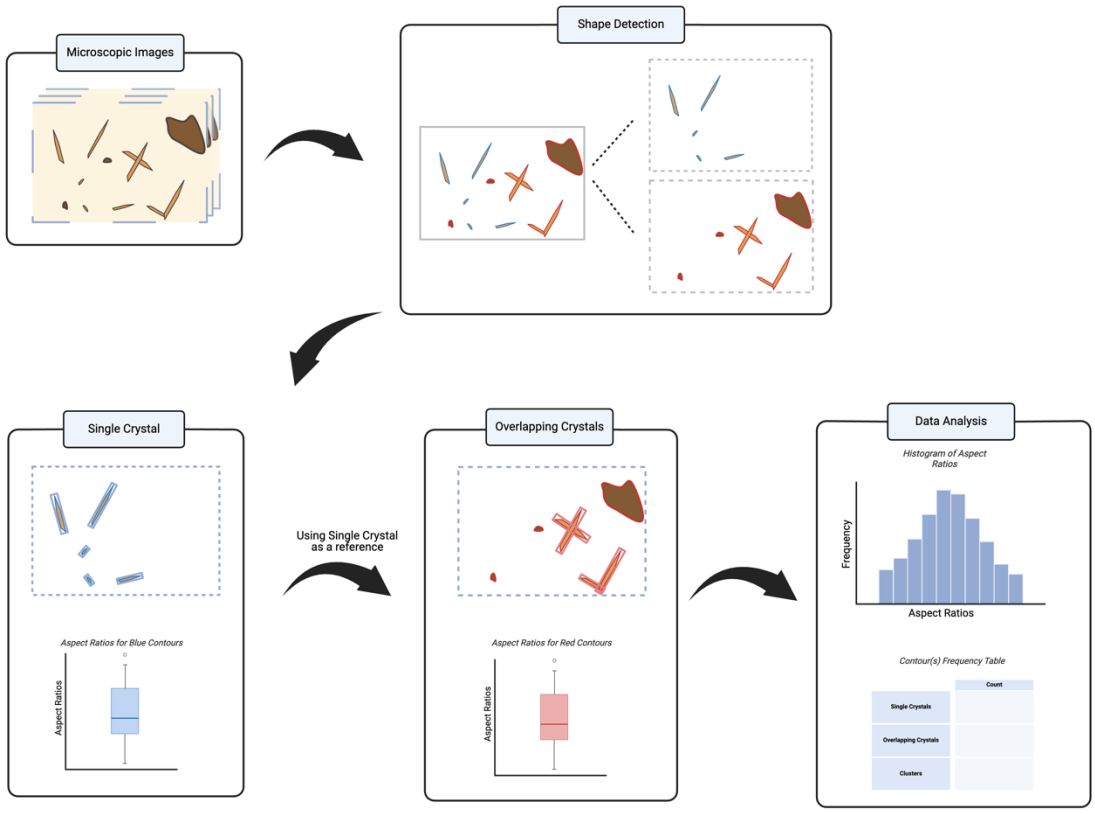

Figure 14 shows the workflow of the machine-learning algorithm Bok Choy that can be used in Python to accelerate characterizing crystals and calculating their ARs.

In Figure 14, *Bok Choy* workflow is outlined as it calculates MOFs ARs with simple Python command runs. Firstly, microscopy images are processed by having their file paths called by the command line and essential Python languages and libraries used to identify and detect individual crystal shapes. In doing so, Bok Choy separates and distinguish MOFs by either single or overlapping, clustered regions.

Using more complex algorithms, ARs are calculated for both single crystals and overlapping crystals. The data is then collected, producing histograms and frequency tables to visualize the distribution of ARs processed samples. This integrated analysis provides quantitative perceptions in a timely manner saving time when contrasted to standard software such as *ImageJ*. A detailed example of *Bok Choy* can be found in Appendix A.

Experimental design and timeline

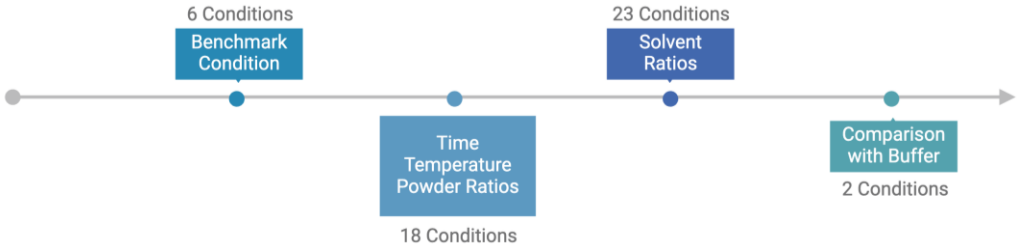

Figure 15 shows the timeline for the experiments done during this research project.

As depicted in Figure 15, the investigational workflow for amalgamating MOFs was guided through a series of methodically diverse conditions. The analysis began with six conditions, which were conducted with the original solvent ratios (1:1:1) of (water:DMF:ethanol) as well as five other random solvent proportions serving as a mock experiment to observe initial trends of ARs. Nonetheless, no clear trends were observed. Therefore, these were followed by an examination of 18 conditions that varied with key factors such as reaction time, temperature, and metal-linker powder proportions, to evaluate their influence on crystal AR.

Afterward, 23 additional conditions focused on changing solvent ratios were explored to find the trends of AR changes with respect to varying defined solvents earlier. This phase offered critical comprehensions into the influence of solvent composition on crystal growth and AR. Lastly, the best two conditions from the 23 were repeated with 4-morpholinepropanesulfonic acid (MOPS)-based buffer to compare buffer vs. non-buffer effects on ARs.

Despite the extensive investigation of numerous conditions, there can be further examination to allow for finding more optimized conditions and clearer trends of AR changes associated with solvent proportions or varying the other key factors. Therefore, this development of tests is far from a complete assessment of variables influencing MOF synthesis, hindering the arrival at the perfect optimization of conditions tailored to obtain the best ARs.

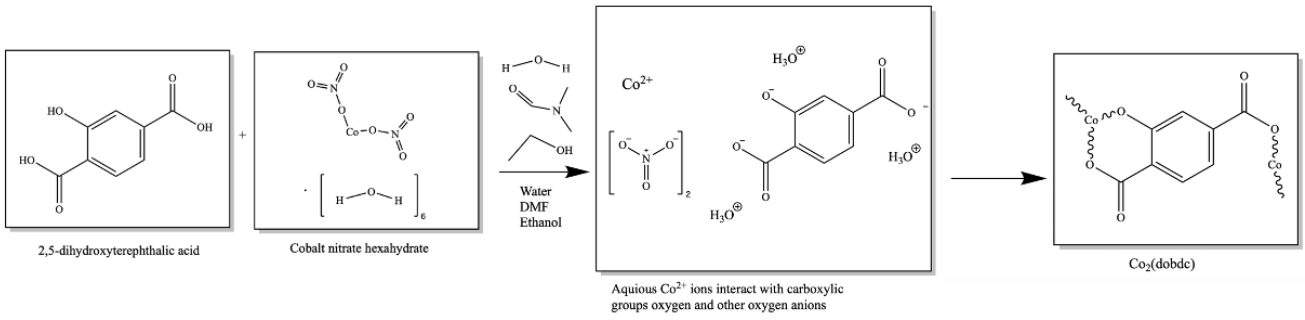

This Project

Figure 16 shows the changes that occurs to the molecules of the chemicals and the reaction that leads to the formation of Co_2(dobdc).

During the synthesis of Co_2(dobdc), a series of deprotonations happen as added chemicals mix quickly producing intermediate molecular components. As intermediate are free to interact, Co^{2+} ions and carboxylic O^- anions bond together to make Co_2(dobdc) in a simple manner.

Detected Impurity

Unfortunately, some side products were evident (Figure 17) in our final products in a couple of the first batch samples. Therefore, we wanted to confirm the identity of these impurities and found that cobalt formate was the most likely to be synthesized according to the following mechanism in Figure 20.

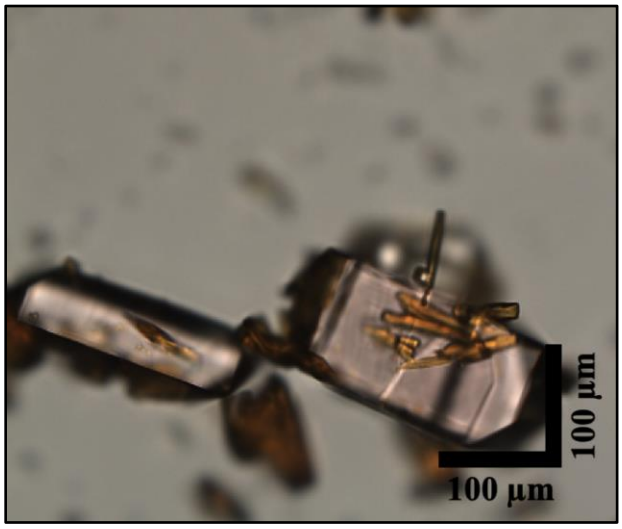

Figure 17 shows detected impurities of cobalt formate in one of the samples from the first batch made with condtion 1I.

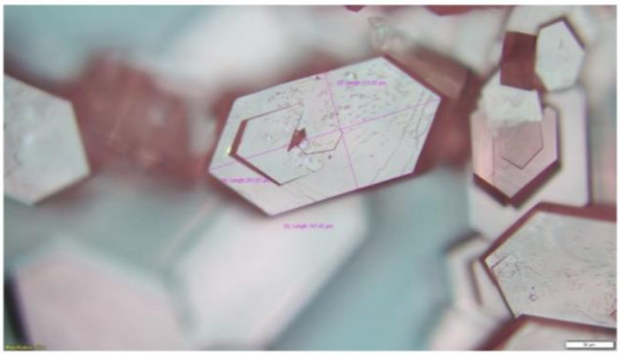

Figure 18 shows the Marimuthu et al.'s synthesized cobalt formate crystals with a white scale bar of 50 um.

As shown in the image in Figure 18, the impurity exhibits a distinctive crystalline morphology with a purple-pink color, divergent from the main target crystals shape, size and color. After prolonged research, these characteristics were found to describe cobalt formate crystals as reported by Marimuthu et al. (2024) in Figure 18. The similarities in the shape are almost identical between in lab synthesized cobalt formate and those reported in literature as noticed by the piercing edges and faceted growth patterns. This observation made our target easier to identify and added more room for analytical insights for what could drive production of impurities, which was later correlated with higher DMF and ethanol proportions and prolonged heating.

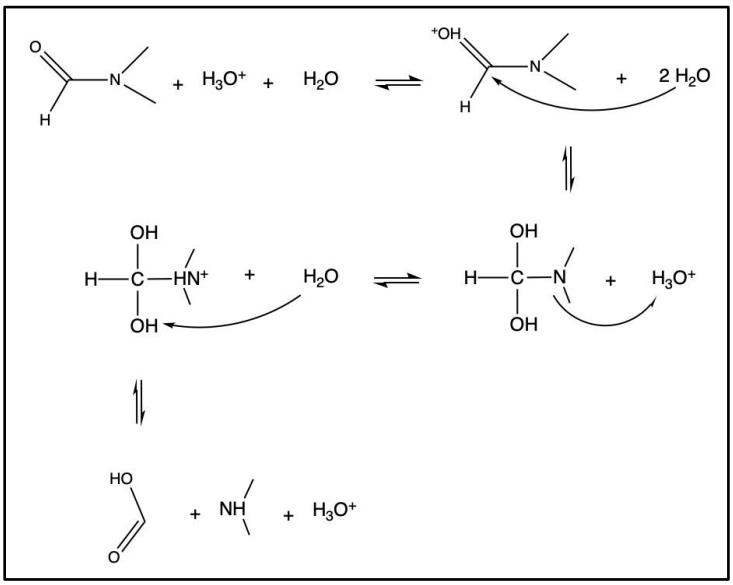

Figure 19 shows the decomposition of DMF through a series of nucleophilic attacks under basic conditions.

Figure 19 illustrates the decomposition of DMF following nucleophilic attacks of water molecules under basic conditions to yield formic acid. This acid is essential in forming impurities in some synthetic conditions observed in this study as illustrated in Figure 20.

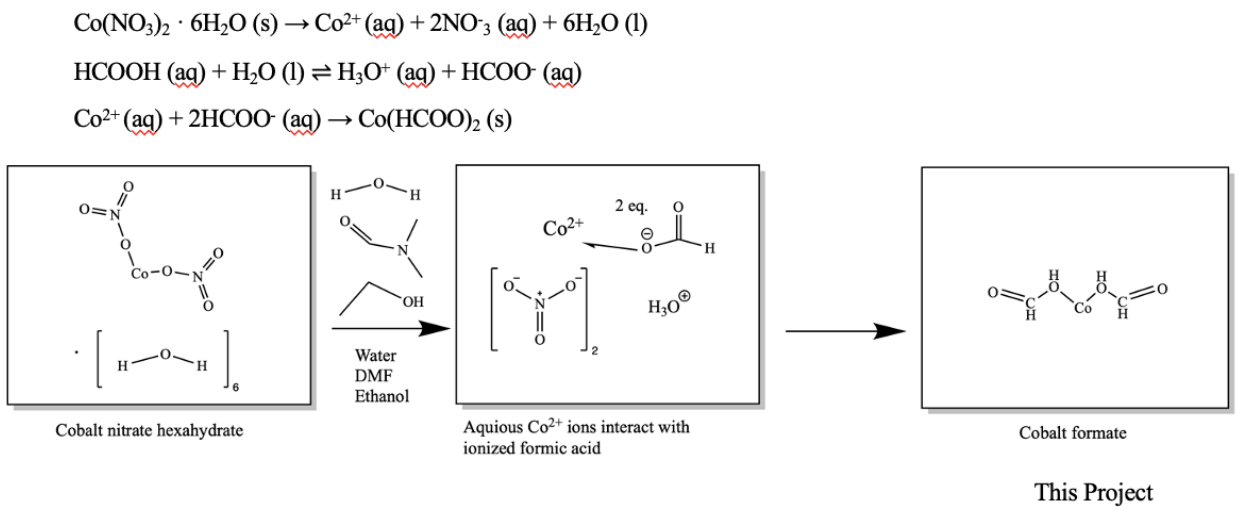

Figure 20 demonstrates equations and schemes that describes the synthesis of cobalt formate.

Figure 20 can be traced to serve as an explanation of the formation of cobalt formate impurities as it shows how ionized formic acid interacts with ionized nitrates to synthesize cobalt formate.

Lab vs. Automated Synthesis

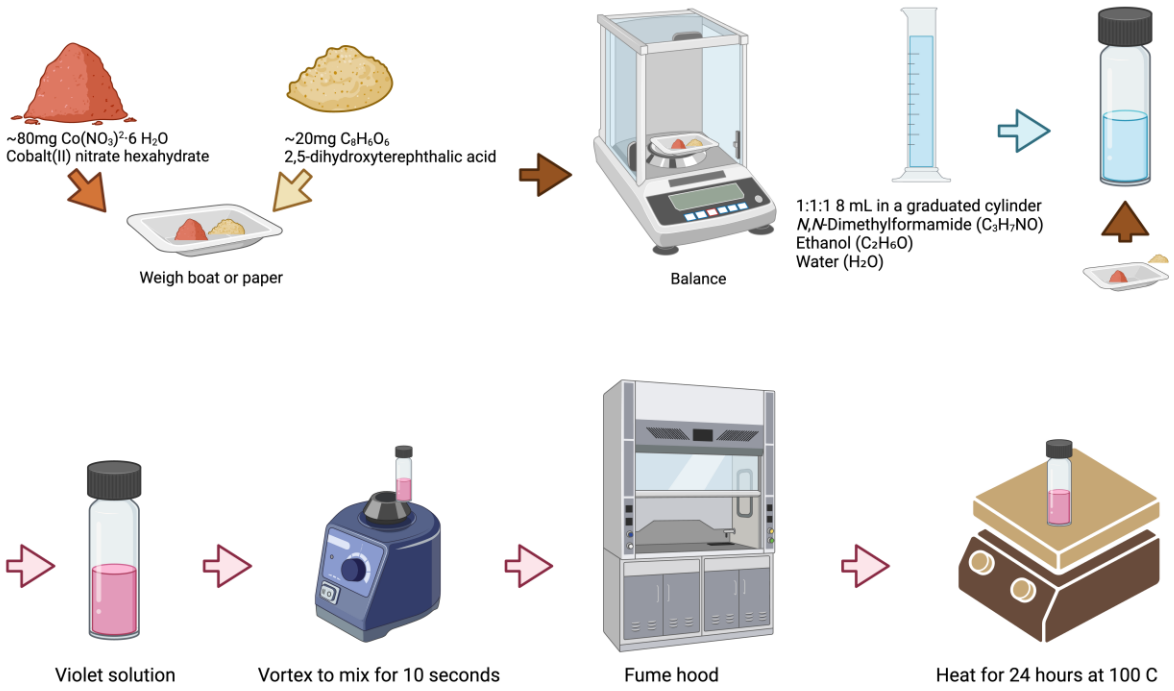

Figure 21 shows the steps to synthesize MOFs with the solvothermal methods using the conventional lab devices.

The production of MOFs involves a series of meticulous steps as illustrated in Figure 21, each demanding precision and time, which features the slow and tedious process. Initially, precise amounts of cobalt (II) nitrate hexahydrate (~80 mg) and 2,5-dihydroxyterephthalic acid (~20 mg) are weighed using a scientific calibrated balance of high accuracy. Then, a solvent mixture in the fume hood is made of *N,N*-dimethylformamide (DMF), ethanol, and water in a 1:1:1 ratio up to 8 or 10 mL total.

The constituents are then combined in a borosilicate scintillation vial dissolving quickly and forming a violet solution. Subsequent thorough mixing with a vortex mixer is performed to ensure homogeneity and remove any remaining chunks. This is important as varying the solvent ratios affects solubility in samples. The ready solution is then moved onto a heater at 100°C for 24 hours.

Every step, from balancing and mixing to prolonged heating, demands cautious attention to detail, leading to time consuming and strenuous process. This emphasizes the need for automation and optimization to streamline synthesis, reduce human error, and accelerate experimental throughput, which is a fundamental purpose of this project.

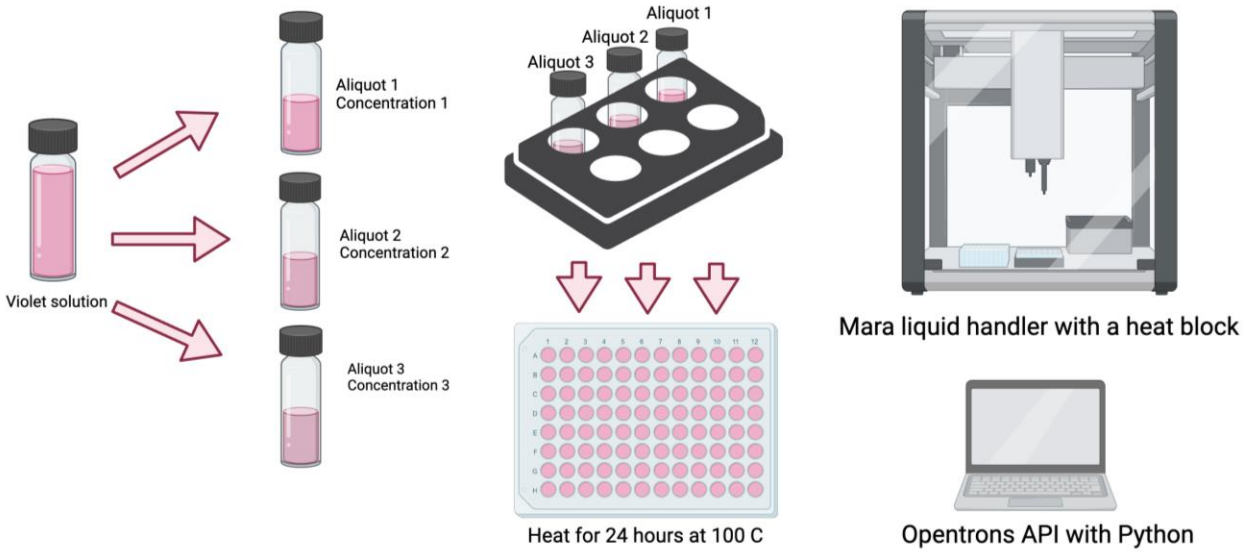

Figure 22 illustrates an example of the automated synthesis used in this project.

Figure 22 shows an example of the automated workflow for synthesizing MOFs using our high-throughput approach. Based on the Python commands, each starting solution can be prepared and aliquots with varying solvent ratios can then be prepared and transferred into well plates for heating, or just heat in vials when needed.

When using well plates, *Mara*, integrated with the heating/shaking adapter, automates the exact pipetting of substances and monitors the reaction measurements, including temperature and

time. This automated approach significantly reduces the time and effort required for synthesis, allowing for the simultaneous evaluation of multiple reaction conditions. By leveraging automation, the process ensures consistency and reproducibility, accelerating the optimization of reaction parameters to achieve desired MOF properties. This method overcomes the limitations of traditional, labor-intensive synthesis workflows, making it a influential tool for progressing MOF research.

Results and Discussion

First Experiment: Varying Proportions of DMF, Water, and Ethanol

The first experiment was designed to test the effect of diversifying the proportions of *N,N*-dimethylformamide (DMF), water (DI H_2O), and ethanol (EtOH) on the ARs of Co_2(dobdc). Six different conditions were tried, each with a fixed reaction time of 72 hours and a metal-linker ratio of 4:1 ($Co(NO_3)_2 \cdot 6H_2O$: dobdc acid).

Table 1 shows the initial experiment with the solvent ratios.

Condition	DI H_2O ul	DMF ul	EtOH ul	Time hr	Powder Ratio
1I	3333	3333	3333	72	$Co_2(NO_3)6H_2O$ **4:1** Dobdc Acid
2I	5000	2500	2500	72	
3I	4000	2000	4000	72	
4I	2500	2500	2500	72	
5I	6000	2000	2000	72	
6I	2500	5000	2500	72	

Condition 3I, consisting of a solvent mixture of 2:1:2 water:DMF:ethanol synthesized crystals with the lowest AR, as highlighted in the ternary plot in Figure 23. This plot visualizes the relationship between solvent composition and AR, with lower values represented by darker navy shades. The outcomes propose that solvent compositions are one of the main factors that influence crystal AR, with Condition 3I aiding as the benchmark for the following experimentations.

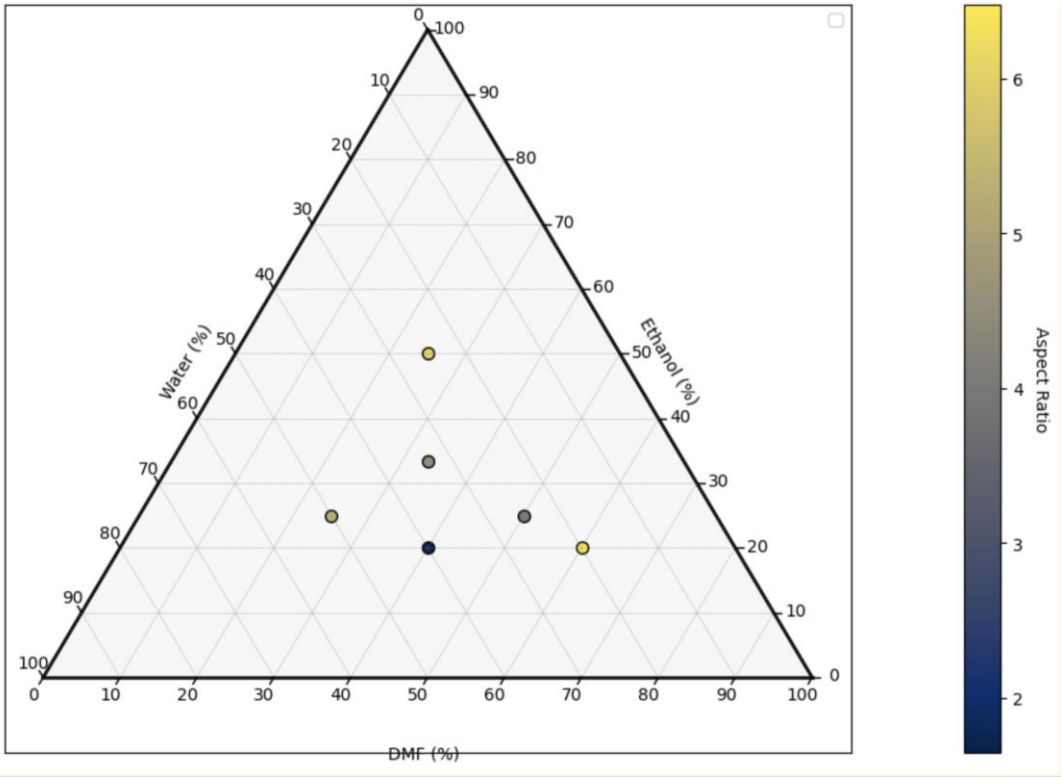

Figure 23 shows a ternary plot with a heat indicator showing the low AR values as dark blue and and high AR values as bright yellow.

That being said, there was no clear trend that associates with solvents, if increased, are more directly responsible for having the lowest ARs as the proportions in 1I to 6I were closely adjusted ad most results showed crystals with long ARs and heterogenous samples.

Orange Crystals Identification with Powder XRD

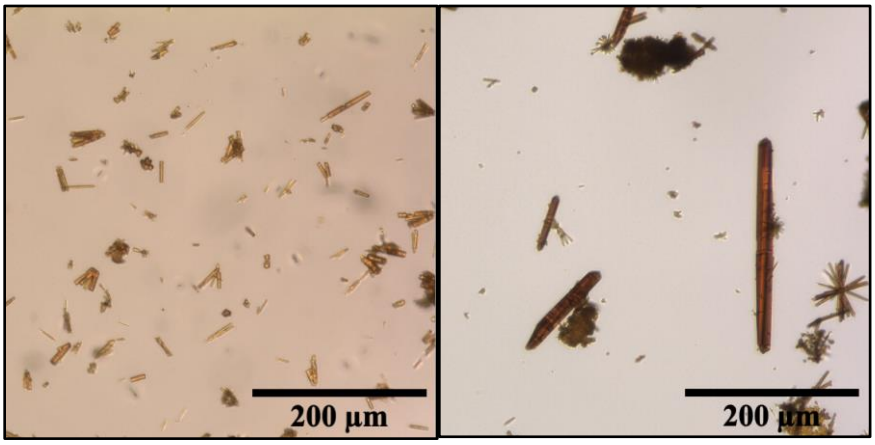

Figure 24 shows two randomly selected samples 1I (left) and 6I (right) to process PXRD.

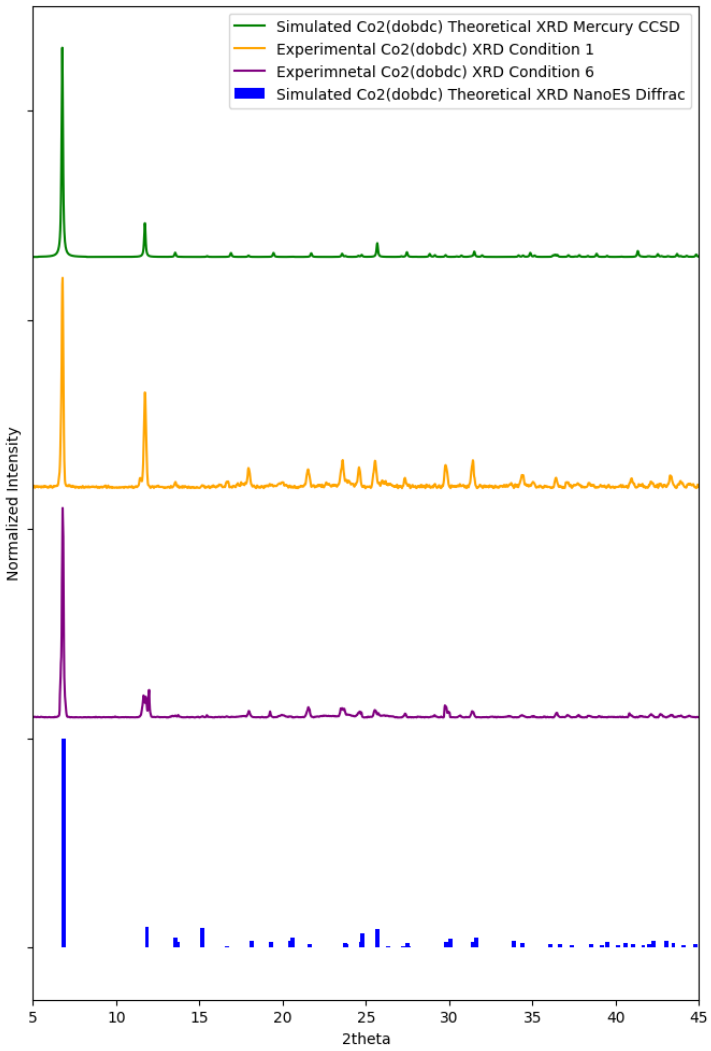

Figure 25 shows matching PXRD patterns for crystals in samples 1I and 6I compared with theoretical, standard and simulated Co_2(dobdc) patterns from credited references.

In an XRD pattern, the x-axis refers to the diffraction angle, denoted as 2θ, which is the angle the separates the incident X-rays and the planes in the crystal matrix. The peaks along this axis refer to the spots of the diffraction maxima, parallel to the exact organization of atoms in the MOF. The y-axis shows the normalized intensity of the diffracted X-rays, with the elevation of each peak reproducing the comparative strength of diffraction from precise crystal surfaces. Therefore, these peaks are used to describe the organization of atoms within the MOF.

The identity of the orange crystals synthesized under Conditions 1 and 6 was confirmed using two XRD analyses in the MAF center. Microscopic images in Figure 24 disclose comparable structural alterations between Condition 1I producing smaller needle-like crystals, whereas Condition 6I larger yet longer crystals. However, both constellations of crystals shared the same orange characterizing color and long ARs.

XRD patterns in Figure 25 were gathered for both conditions and compared to simulated theoretical data for Co_2(dobdc) from the UW NanoES and the Cambridge Crystallographic Data

Centre (CCSD) database. Notably, both experimental XRD patterns matched with the simulated ones, confirming the synthesis of the desired Co_2(dobdc). Thus, we established that using both microscopy and XRD were essential for verifying having the correct MOFs.

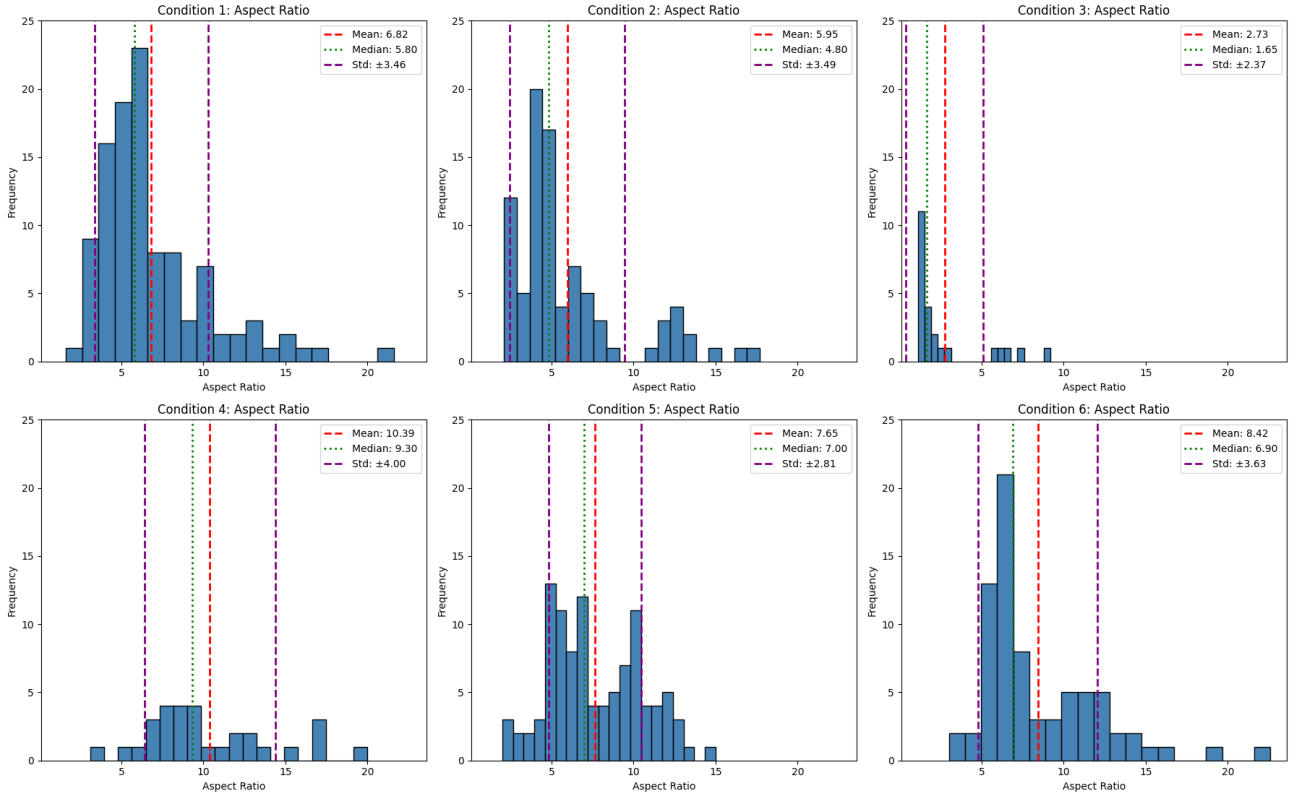

Figure 26 shows histograms for the ARs corresponding to conditions 1I through 6I, calculated with ImageJ.

Using *ImageJ*, the ARs of individual crystals were quantified as shown in Figure 26 and represented by the x-axis, and the frequency on the y-axis refers to the number of crystals that were found to have a defined AR.

Condition 3I showed the smallest average AR, 2.73, and median AR, 1.65, with the least standard deviation, depicting more uniform and homogenous crystals. Conversely, Conditions 4I and 6I had relatively greater average ARs of 10.39 and 8.42, respectively. Conditions 1I, 2I, and 5I showed relatively great ARs as well, with varying standard deviations that reflect the heterogeneity of the samples and the larger distribution. Ultimately, these histograms emphasize the sensitivity of crystal ARs to solvent proportions in every sample.

Preliminary Results Using the Naive Bok Choy Algorithm

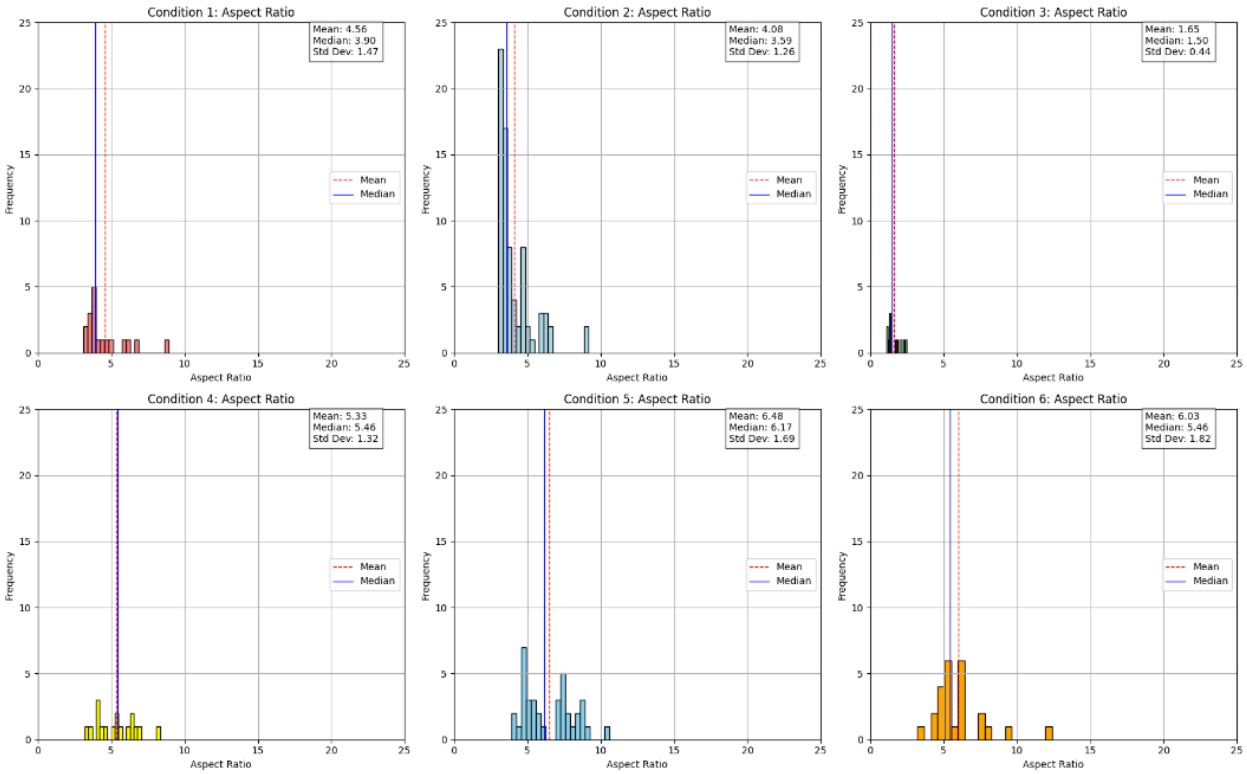

Figure 27 shows histograms for the ARs corresponding to conditions 1I through 6I, calculated with Bok Choy.

These histograms in Figure 27 show the AR distributions of MOFs quantified of the same first batch of the 1I-6I conditions using the first naive version of the *Bok Choy* algorithm, before further refinements were implemented.

This initial quantification showed that condition 3I still was associated with the lowest average AR, 3.05, and median, 2.50, with a standard deviation of 0.44 indicating the lowest variation in the sample. Contrarywise, other conditions, such as condition 1I with a mean AR of 13.5, and condition 4I with a mean of 5.3 were still associated with greater ARs and broader distributions, reflecting the elongated and needle appearances of crystals.

Despite showing a similar trend to that of *ImageJ*, *Bok Choy* algorithm clearly required further adjustments discussed in Appendix A and used for characterizing the ARs in the other experiments. Fortunately, the following experiments witnessed less impurities in general as well as improved microscopic imaging especially with solving the shortcomings such as recurrent overlapping crystals by means of excessive dilution post-crystallization.

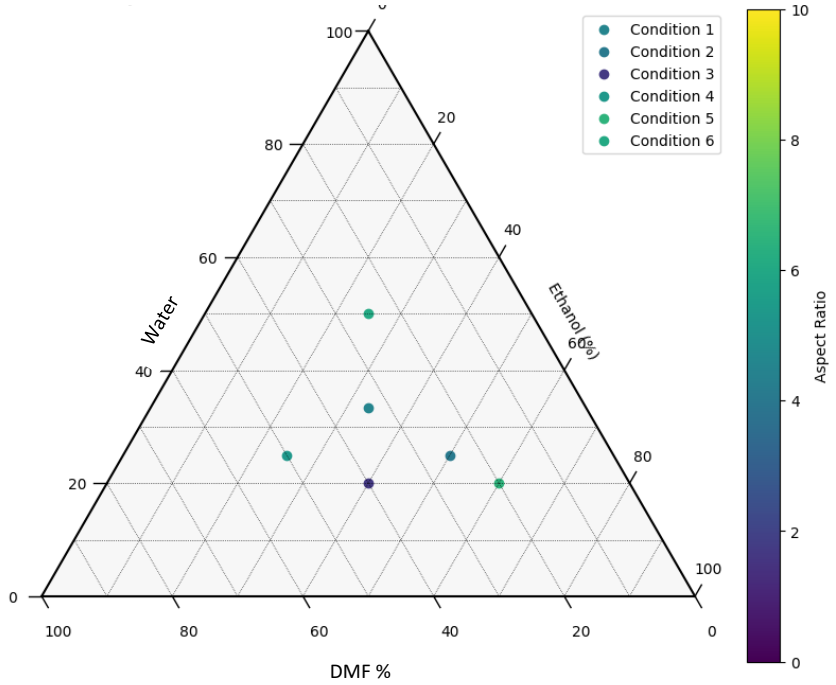

Figure 28 shows ternary plots for the Bok Choy quantifications to reveal trends between ARs and solvent proportions.

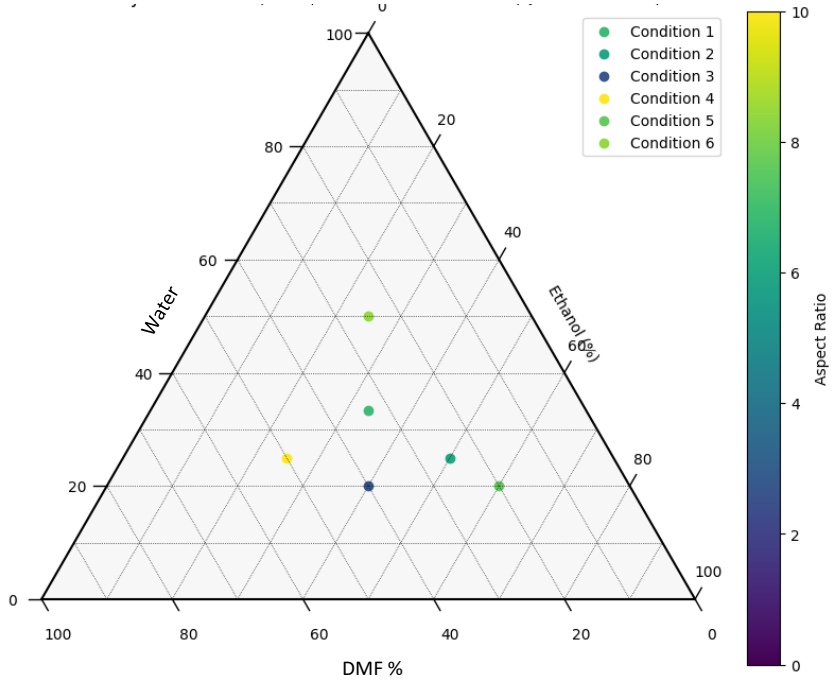

Figure 29 shows ternary plots for the Bok Choy quantifications to reveal trends between ARs and solvent proportions.

The ternary plots in Figures 28 and 29 were used to illustrate a comparison of ARs measured of the same conditions using *Bok Choy* algorithm and *ImageJ* to test how solvent proportions affected the ARs obtained.

This assessment authenticates the strength of the *Bok Choy* algorithm while indicating consistency with results obtained using the established *ImageJ* software. The similarity in both trends assert that both software effectively grasp the impact of solvent proportions on MOF ARs. Subsequent modifications of *Bok Choy* further diminished incongruities, enhancing accuracy in automated crystal analysis.

Comparison of AR Calculations for Single and Overlapping Crystals

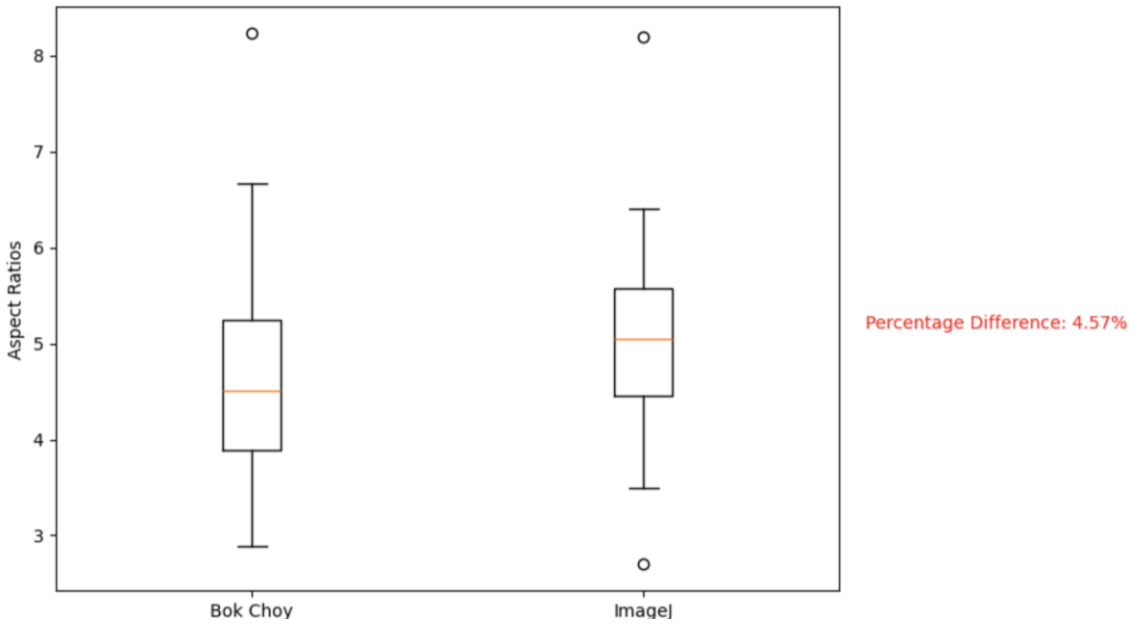

Figure 30 shows the quantified ARs of randomly selected single non-overlapping crystals using Bok Choy (left) and ImageJ (right) with a slight percent difference between the two.

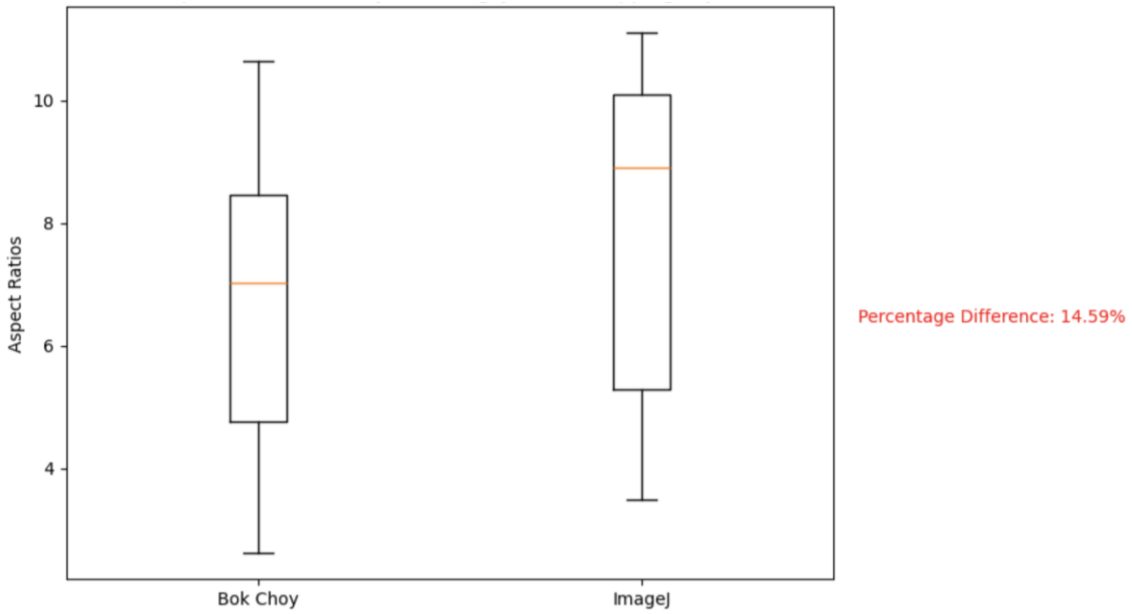

Figure 31 shows the quantified ARs of randomly selected overlapping crystals using Bok Choy (left) and ImageJ (right) with a great percent difference between the two.

Two analyses in Figures 30 and 31 compared the quantifications of ARs as detected for single and overlapping crystals via *Bok Choy* and *ImageJ*. The box plots uncover a strong match between the two software results for detecting single crystals ARs, with a percentage difference of about 4.57%. Such a consistency highlights the dependability of both in analyzing isolated MOFs.

Conversely, for overlapping MOFs, the percentage difference between *Bok Choy* and *ImageJ* upsurges significantly to nearly 14.59%. This inconsistency replicates the obstacles both tools encounter while detecting and measuring ARs for overlapping crystals that dimmish the precision and accuracy of obtained measurements.

Due to the greater reliability observed for detecting single crystals, we elected to only use single isolated crystal measurements of ARs using *Bok Choy*. Such a strategy ensures higher accuracy and consistency in our analysis and interpretation of results, eliminating the caveat of including the measurements of the overlapping crystals that would add more complexities and additional errors. These conclusions assert the significance of further refining *Bok Choy* for the overlapping regions as well as slightly less importantly for the single non-overlapping ones to make the percentage differences closer to zero.

Second Experiment: Temperature Changes Affecting Crystal Size and AR

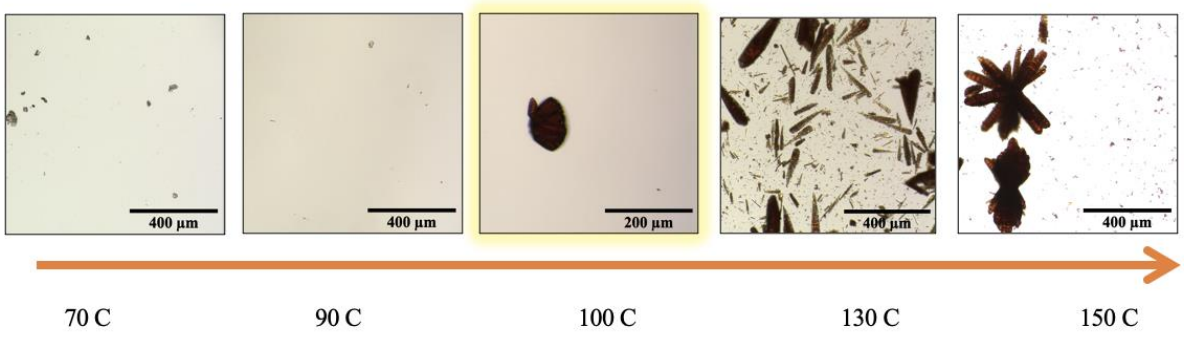

Figure 32 shows the effect of changing temperatures on the ARs of obtained MOFs.

The second experiment is depicted in Figure 32, which investigates the effect of elevating reaction temperatures, from 70°C and up to 150°C, on the ARs of the Co_2(dobdc) MOFs, synthesized under consistent solvent proportions as in condition 3I (2:1:2 ratio of water, DMF, and ethanol) and a reaction time of 24 hours. The images exemplify the development of crystallization as the temperature elevates, which is congruent with the expected hypothesis of having larger and elongated particles.

At lower temperatures (70°C and 90°C), there were no crystals or precursors showing, suggesting inadequate thermal energy for any nucleation. At 100°C, the highlighted sample crystal from 3I was used as a reference that shows a well-defined, compact crystal with near ideal AR. At highly elevated temperatures, 130°C and 150°C, crystal growth becomes significant yet crooked, with elongated, overlapping and accumulating crystals, which is consistent with expected patterns. The outcomes highlight that 100°C is the most critical temperature for synthesizing Co_2(dobdc) MOFs without compromising the homogeneity and desirable AR range. Such findings further illustrate how essential it is to keep attempting fine-tuning reaction parameters to hone down the range of ARs obtained to eventually optimize MOF performance in their applications.

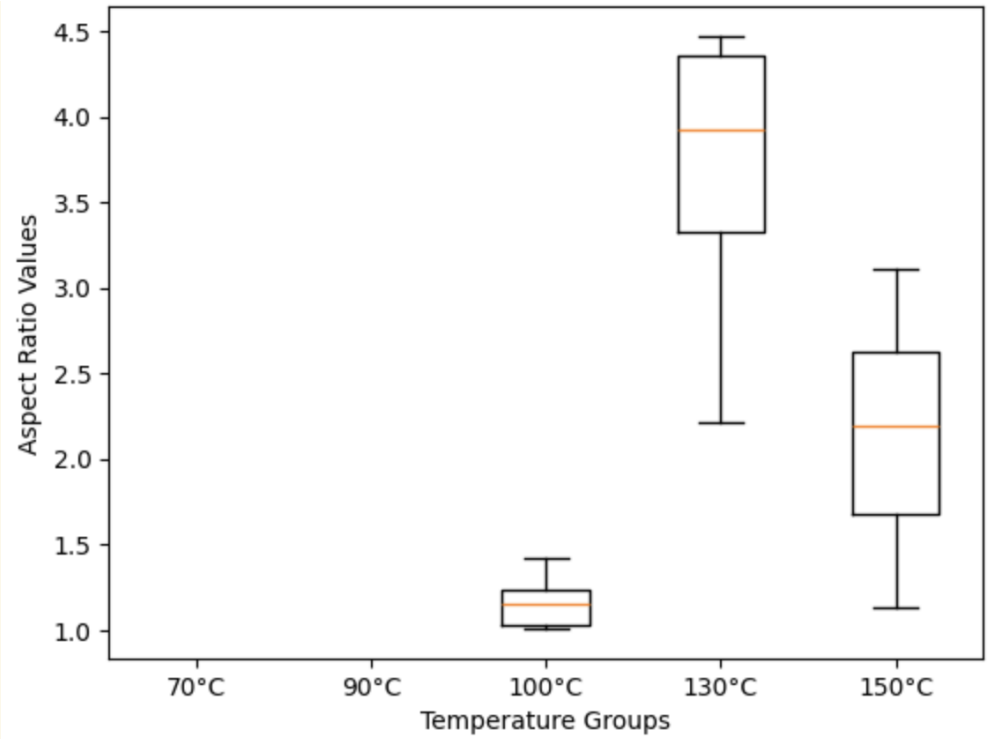

Figure 33 shows box plots that quantify AR medians and ranges from the samples associated with the temperature elevation experiment.

The difference of crystal ARs with elevating reaction temperature is illustrated in the box plot in Figure 33. The data features a clear relationship between temperature and AR. At 70°C and 90°C, the AR value is zero, representing the absence of any formation. The optimal temperature of 100°C exhibits the lowest AR values with close minimal and maximal whiskers, indicating more homogenous and isotropic crystallization.

As the temperature increases to 130°C, a major increase in AR is detected, accompanied by a wider distribution as the whiskers go further apart. This suggests the onset of heterogeneous crystallization, containing elongated as well as irregular crystals. At 150°C, the AR values stay elevated but show a narrower spread compared to 130°C as whiskers seem relatively closer, probably due to excessive nucleation leading at higher thermal energy levels.

Such a trend depicts how this experiment is congruent with the non-classical crystallization theory discussed earlier and asserts how essential temperature is maintaining crystallization to attain desirable crystal morphologies with low AR and homogeneity in MOF synthesis.

Third Experiment: Effect of Reaction Time on Crystal Size and Morphology

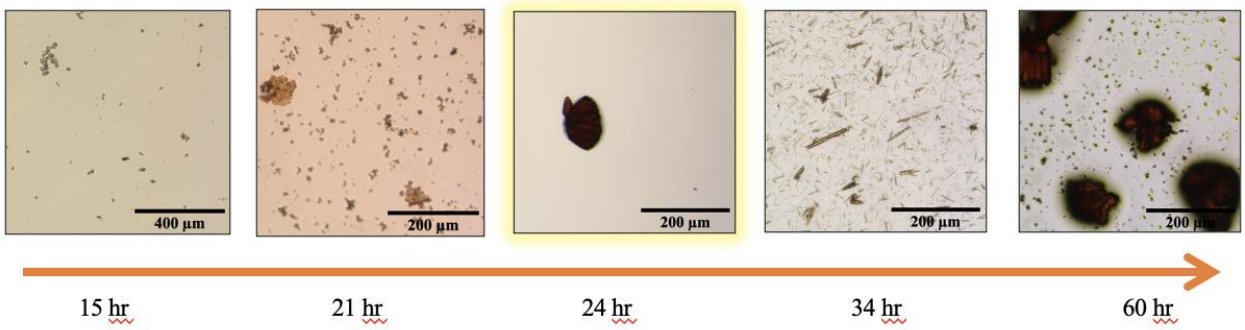

Figure 34 shows the effect of increasing synthesis time on the ARs of the MOFs.

The third experiment discovers the impact of varying reaction duration from 15 hours and up to 60 hours on the ARs of Co_2(dobdc) MOFs synthesized under 3I of defined temperatures and initial proportions. The development of crystallization over time is revealed in the microscopic images in Figure 34, which is also congruent with literature reviews and expected patterns.

At 15 and 21 hours, there were no crystals detected, and the observed entities could be attributed as small pre-nuclei, revealing incomplete crystallization. Lengthening the reaction time past 24 hours, such as 34 and 60 hours, leads to heterogenous and higher AR crystals in addition to remarkable overlapping and saturation.

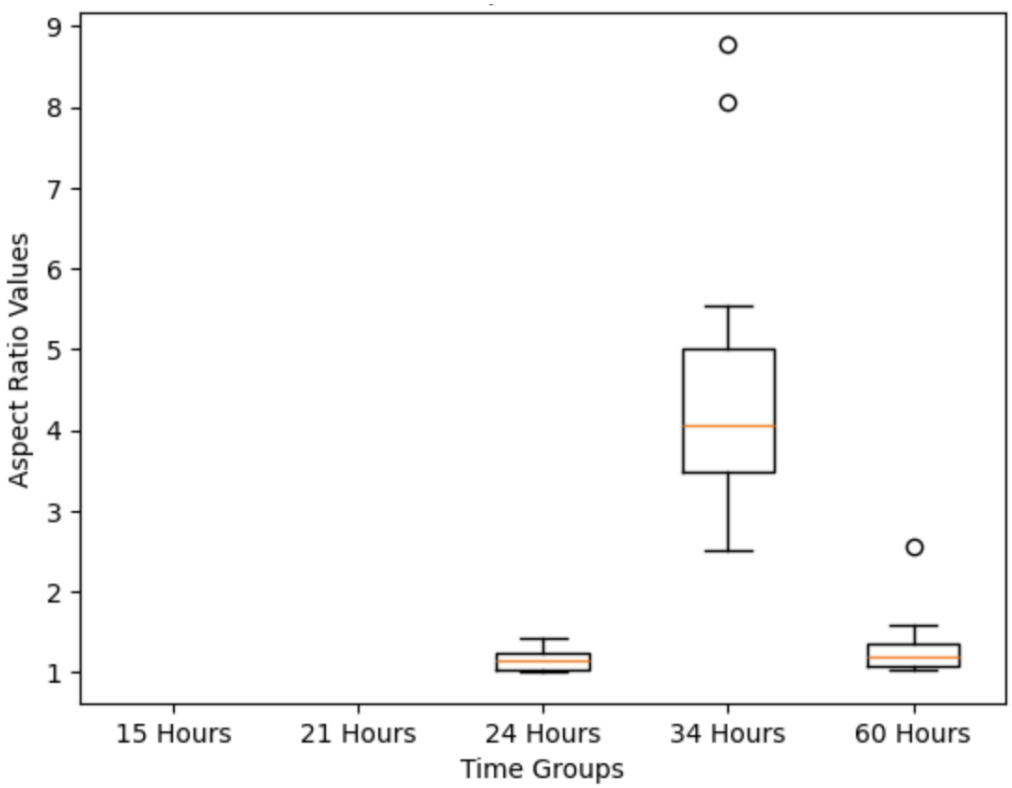

Figure 35 shows the box plots for the quantified ARs in the time experiment.

The box plot in Figure 35 illustrates how reaction time affects the ARs of Co_2(dobdc) crystals. At 15 and 21 hours, the AR values zeros due to no formation, though there were some sheet-like pre-nuclei formed. At 24 hours, the AR values are low with minimal variation as the whiskers look closely distanced.

At 34 hours, a significant increase in AR is witnessed. This is associated with more stretched and pointed crystals. Using 60 hours, the AR values decrease slightly, but aggregation was dominating in this sample leading to absence of homogeneity in crystal AR.

These results from the third experiment accentuate the critical role of reaction time in governing crystal growth and morphology with desirable ARs. The optimal reaction time of 24 hours balances nucleation and growth, creating more uniform crystals with less aggregation. Extended reaction times seem to augment energy levels and boost further crystallization that compromise crystal quality.

Fourth Experiment: Varying Metal-Modulator ($Co(NO_3)_2 \cdot 6H_2O$) Quantity

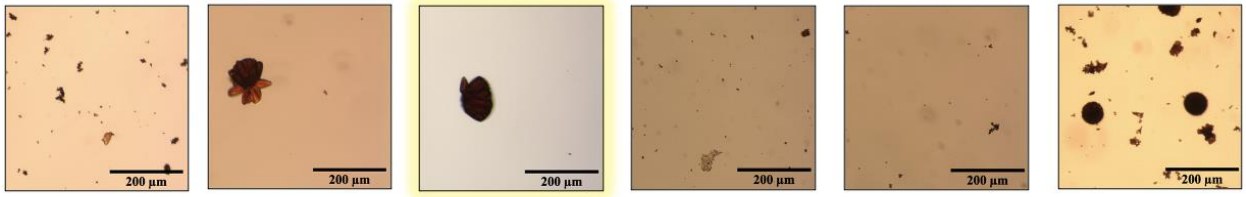

Figure 36 shows the effect of varying the metal source proportions on the ARs of the synthesized crystals.

The fourth experiment investigates the influence of varying the metal-to-linker ratio on the morphology and ARs of Co_2(dobdc) crystals. As the metal-modulator ratio changes incrementally from 3.4:1 to 4.8:1, distinct differences in crystal AR and uniformity are observed in Figure 36.

At a ratio of 3.4:1, no crystallization was observed and only pre-nuclei sheets formed, suggesting deficient coordination between the metal ions and ligands. At 3.7:1, more uniform crystals were observed, with more defining features. The crystallization at the optimized ratio of 4:1 was discussed earlier.

Beyond the conventional ratio, at 4.3:1 and 4.6:1, no crystallization was observed and only pre-nuclei sheets appeared, likely due to weak solubility with increasing initial metal source. Using 4.8:1, substantial accumulation and non-uniform particles appear as well as some crystals forming a rose like crystal with rods extending from the center shared by such crystals.

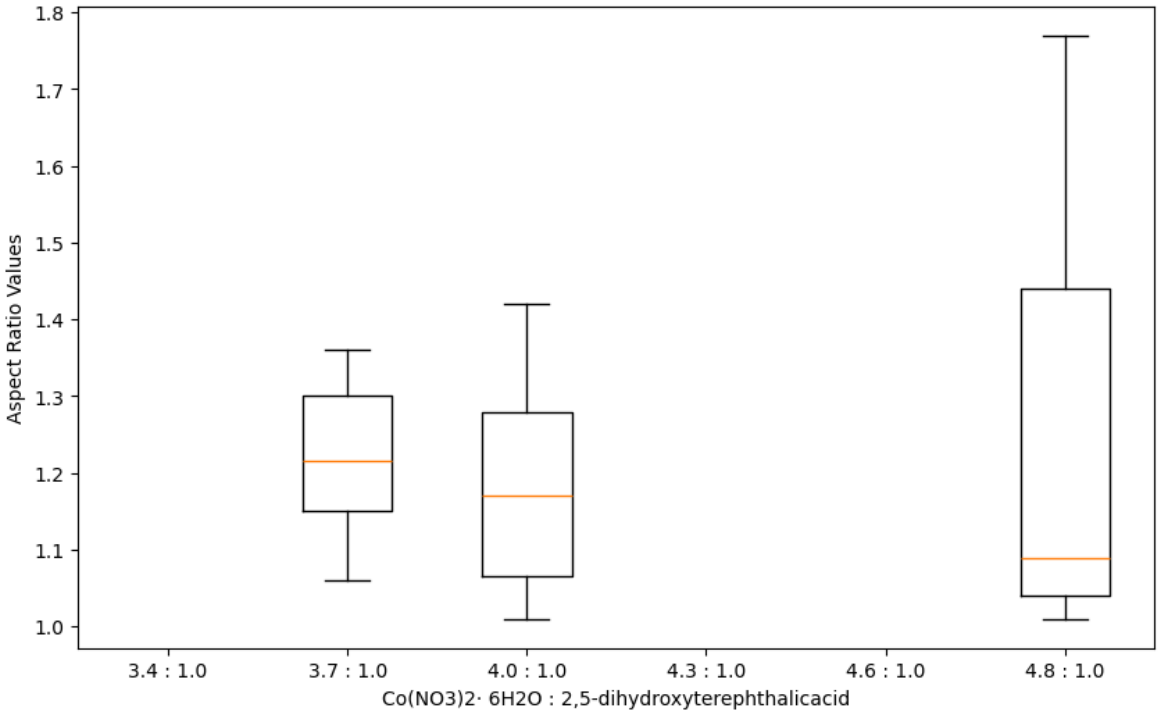

Figure 37 shows the box plots associated with varying the metal source experiment.

The changes in ARs observed in the fourth experiment offers a strong quantitative standpoint on the effect of the metal-to-modulator ratio. The box plot in Figure 37 illustrates how increasing the ratio of $Co(NO_3)_2 \cdot 6H_2O$ to 2,5-dihydroxyterephthalic acid affects the AR of Co_2(dobdc) MOFs.

At 3.4:1, the AR is zero due to no crystallization. At 3.7:1, the AR are comparable to that of the optimal 4:1, with closely juxtaposed median value and similar range of variation. At 4.3:1 and 4.6:1, the AR values are zeros due to absence of crystals and dominance of pre-nuclei sheets.

By 4.8:1, the AR distribution broadens significantly, indicating the emergence of irregular crystal structures and agglomeration. The increasing AR at higher ratios reflects a disruption in coordination chemistry, which hinders uniform crystal growth.

This experimentation accentuates that varying the metal-modulator adds irregularities to the final sample whereas using the original recipe maintains ideal formation, confirming that precise stoichiometric control is essential for MOF synthesis. The deviations, clearly, disturb the homogeneity of the samples or lead to preventing crystallization.

Fourth Experiment: Varying Linker (2,5-Dihydroxyterephthalic Acid) Quantity

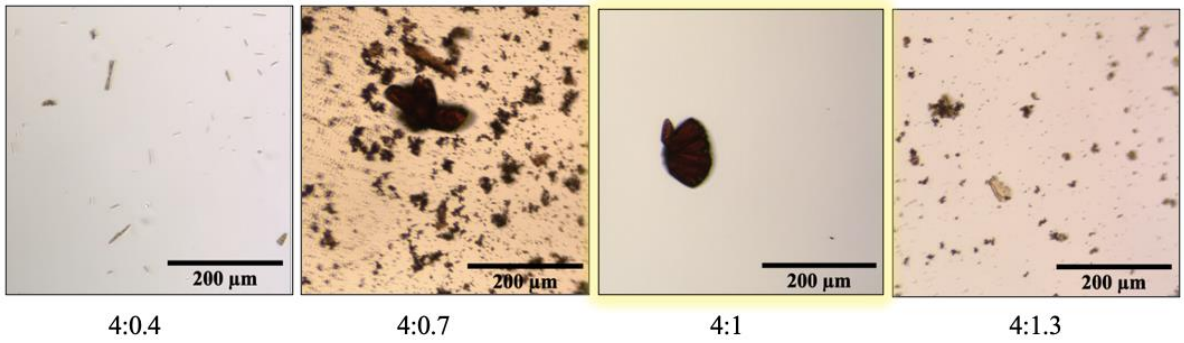

Figure 38 shows the effect of varying the linker proportions on the ARs on the synthesized crystals.

The fourth experiment discovers the impact of varying the quantity of the linker, 2,5-dihydroxyterephthalic acid, on crystal morphology and AR. By systematically changing the linker-to-metal ratio, distinctive tendencies in crystal development were observed in Figure 38.

At 4:0.4, scarce crystallization was observed. At 4:0.7, the resulting crystals were also poor and difficult to find with irregular shapes and significantly higher levels of pre-nuclei sheets, likely due to incomplete coordination between aqueous ions. These conditions clearly fail to stimulate adequate crystallization, as the available linker molecules are deficient to endure proper MOF assembly.

The optimal condition of 4:1 ratio was discussed earlier, where well-defined MOF features can be attributed to adequate coordination between the aqueous metal centers and linker molecules roaming in the sample, enabling the construction of a steady and coherent crystal structure.

Using 4:1.3, the system becomes oversaturated, synthesizing pre-nuclei sheets and irregularities due to imperfect coordination between ions. These higher ratios of the linker as in 4:1.6 and 4:1.9 disturb the orderliness of the crystal matrix, compromising the ability to sustain the crystallization process.

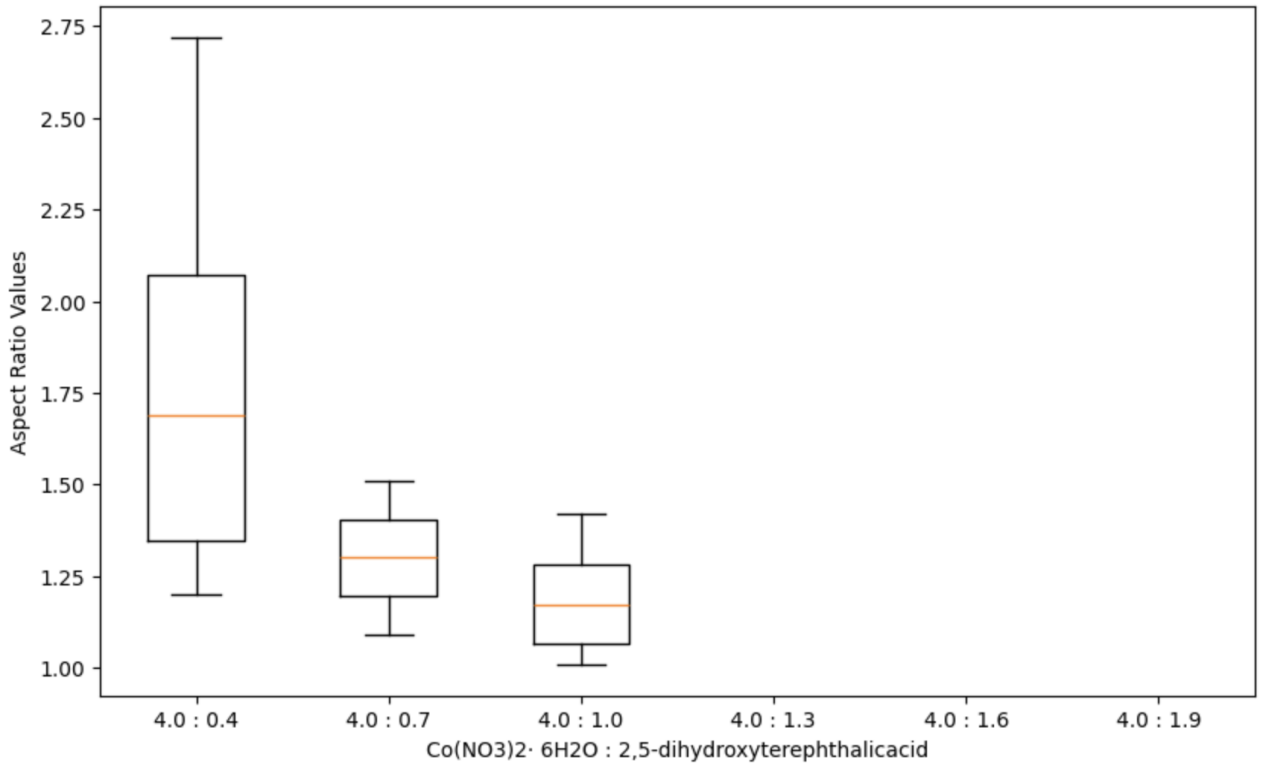

Figure 39 shows the box plots associated with varying the linker source experiment.

The boxplot analysis in Figure 39 of varying 2,5-dihydroxyterephthalic acid (linker) quantities reveals its significant impact on the AR of Co_2(dobdc) crystals. Lower linker ratios resembled by 4:0.4 and 4:0.7 were associated with variations in the sample due to the wide separation between and top and bottom whisker ends, indicating that the frameworks need little amounts of linker proportions to start forming. At 4:1, a strong reduction in AR inconsistency is observed, and the crystals were found more homogenous, corresponding to the ideal stoichiometric balance. Nevertheless, as the linker ratio increases beyond this ratio, AR values become zeros due to no crystallizations in all these samples. This outcome highlights the critical role of precise stoichiometry in synthesizing high-quality particles with desirable AR.

Fifth Experiment: Using Condition 3I as a Benchmark for 23 Conditions with Varying Solvent Volumes

Table 2 shows the parameters changed for generating the largest batch in the experimental series for samples 1II to 23II.

Condition Set	DI H_2O	DMF	EtOH	Duration	Monitor
H_2O constant, changing DMF and EtOH	4000 uL (constant)	1000 uL -> 6000 uL	1000 uL -> 6000 uL	24 hours	Solubility
DMF constant, changing H_2O and EtOH	1000 uL -> 6000 uL	4000 uL (constant)	1000 uL -> 6000 uL	24 hours	Crystallization
Ethanol constant, changing H_2O and DMF	1000 uL -> 6000 uL	1000 uL -> 6000 uL	4000 uL (constant)	24 hours	Aspect ratio

The fifth experiment uses condition 3I as a benchmark to explore 23 forms by varying solvent volumes as shown in Table 2. Three sets of experiments were designed to investigated and solubility, crystallization, and AR of Co_2(dobdc) crystals were monitored.

In the first set, the water volume was held constant at 4000 µL while DMF and ethanol volumes were varied from 1000 µL to 6000 µL.

In the second set, DMF was maintained constant at 4000 µL, and water and ethanol were varied to study crystallization behavior.

Finally, the third set fixed ethanol at 4000 µL while water and DMF were adjusted, planning to assess alterations in ARs.

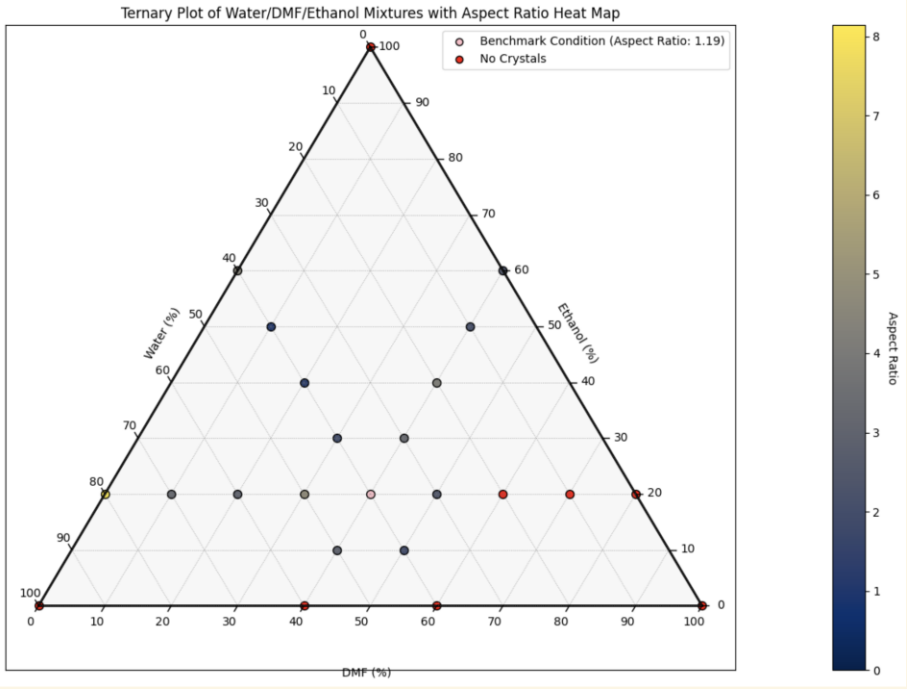

Figure 40 shows the ternary plot with the corresponding heat bar indicator that refers to AR values.

The ternary plot in Figure 40 illustrates the results of 1II through 23II experimental forms involving variations in DI water, DMF, and ethanol volumes. This analysis involved around 700 separate images. The results indicated that reducing DI water volume leads to lower ARs, while high DI water volumes hinder crystal growth. The absence of DMF entirely prevented crystallization, emphasizing its essential involvement in solubility and providing the MOF with the proper environment for successful construction. However, DMF did not interfere while using acetate as a linker as reported in the original Colwell et al. study (2021). In contrast, high ethanol concentrations promoted aggregation, adversely affecting crystal AR. The benchmark condition (AR of 1.19) is highlighted for comparison, providing a reference for optimal crystal formation in top right of Figure 40.

Sixth Experiment: Using 4-Morpholinepropanesulfonic Acid (MOPS)

According to literature reviews done in this study, choosing the most suitable pH value can be essential for obtaining the best ARs (Colwell et al., 2021). Particularly, a neutral value of 7 was found to be the best as only negligible amounts of MOFs become synthesized below a pH of 5 and the probability of forming impurities increase at a pH of 8 (Colwell et al., 2021). Interestingly, using the MOPS-based buffer in the reaction mix led to having smaller crystallites than those obtained while excluding MOPS (Colwell et al., 2021). This suggests that MOPS makes become increasingly competitive for active sites, granting the reaction with additional coordination control for more uniform population of crystallites (Colwell et al., 2021). MOPS inclusion in the mixture offers reliable control over pH values as it does not interact strongly with metals and has a neutral pKa, acid dissociation constant, value of 7.2 (Good et al., 1966).

In the sixth experiment, a 200 mM buffer solution of 4-morpholinepropanesulfonic acid (MOPS) was prepared to repeat conditions 4II and 5II as shown in Table 3, which were both identified as developing the lowest AR from the fifth experiment. The use of MOPS buffer established successful crystallization under both conditions with comparable ARs. This emphasizes that using the buffer helped with enhanced crystallization. The MOPS molecule is shown in Figure 41.

The MOPS buffer solution was prepared using $C_7H_{14}NNaO_4S$ (MOPS sodium salt), with a formula weight of 231.25 g/mol. To create a 200 mM solution, 23.13 g of MOPS sodium salt was dissolved in DI water, and the total volume was adjusted to 500 mL. The initial solution had a pH of 8.6, which was adjusted to pH 7 by adding three drops of HCl. The final buffer contained approximately 100 ppm of ions, representing its difference from DI water with 0 ppm of ions. These ionic interactions provided by integrating the buffer in the mixture are crucial for stabilizing the reaction environment and improving competition to fill all active Co^{2+} sites (Marshall et al., 2019).

Table 3 shows the conditions parameters used for samples 4II and 5II associated with the best ARs.

Condition	Buffer ul	DMF ul	EtOH ul	Duration hr	Powder Ratio	Crystallization
4II	2000	4000	4000	24	4:1	Yes
5II	1000	5000	4000	24	4:1	Yes

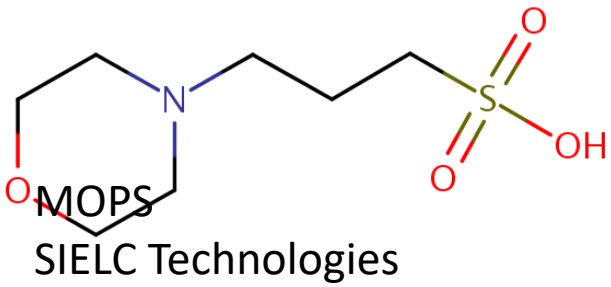

Figure 41 shows the molecule of MOPS.

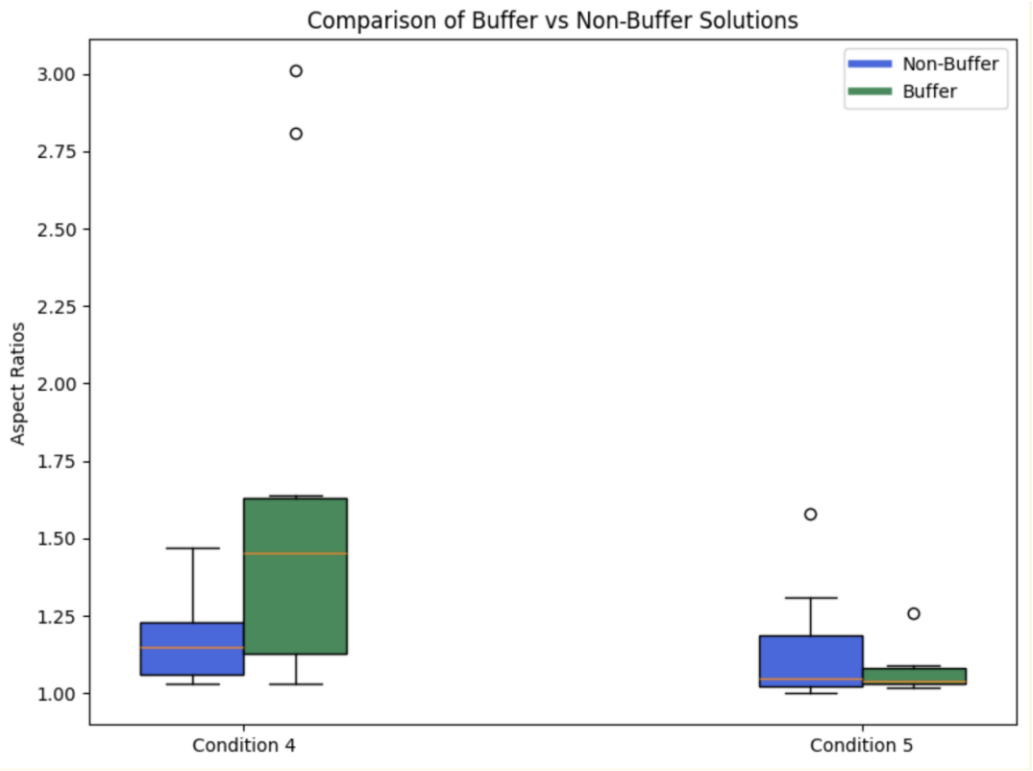

Figure 42 shows the box plots associated with buffered and non-buffered samples of 4II and 5II were there ARs are compared.

The assessment of ARs with and without buffer emphasizes the effect ionic competition to enhance MOF construction. Conditions 4II and 5II were repeated with and without buffer and their ARs were characterized as illustrated in the box plot shown in Figure 42.

The results prove that the presence of the buffer generally led to increased variability in ARs for 4II, yet with negligible median value surge. In contrast, 5II preserved low ARs with even less variability as the distance between the whisker minimum and maximum shrunk with buffer. This further offers that the introduction of buffer in 5II form improved its ARs due to enhanced environment for MOF assembly. Overall, this experiment proposes that while buffers can enhance ionic interactions in some schemes, their impact may vary based on the specific crystallization parameters or initial mixtures.

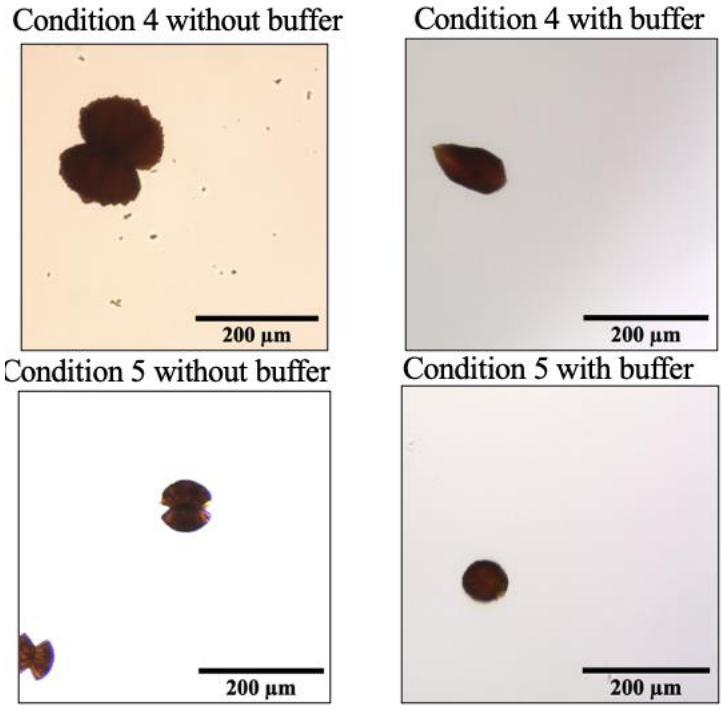

Figure 43 shows exemplary crystals for illustrated optimal conditions.

The images in Figure 43 compare the crystal ARs for 4II and 5II with and without the use of MOPS-based buffer. For 4II, including buffer in the initial mixture seems to improve the crystal shape as the figure in the left may be clustered MOFs and the one to the right appears to be one entity of MOFs. For 5II, the ARs were obviously improved with the addition of buffer. Such an observation supports the quantitative data, highlighting the buffer's role in influencing ionic exchanges and stimulating improved crystal AR.

Summary of Conditions and Estimated Processing Time

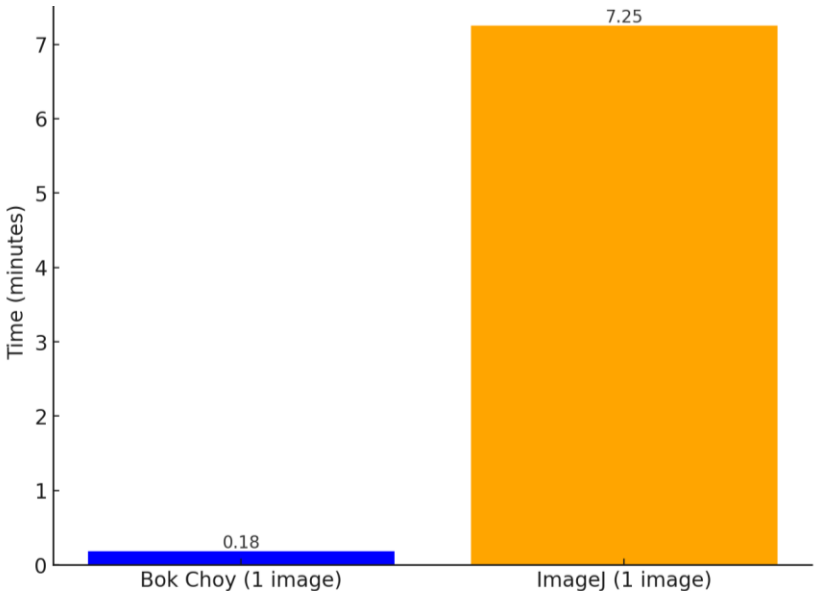

Figure 44 shows the relative duration to complete analyzing a set of crystals in one image using both software.

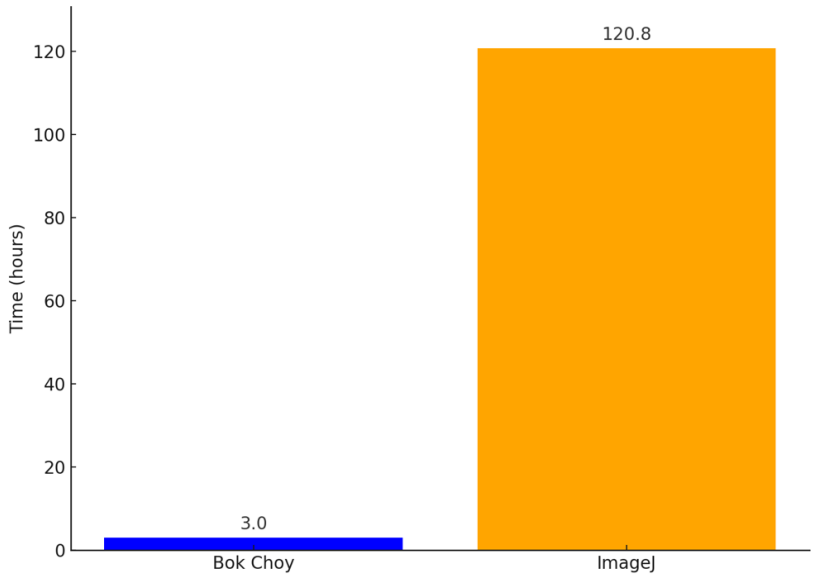

Figure 45 shows the relative duration to complete analyzing a set of crystals in 1,000 images using both software.

Figure 44 and 45 summarized the processing time needed for characterizing MOFs using *Bok Choy* algorithm compared to the commonly used *ImageJ* tool to investigate particles. Across a dataset of 1000 images representing about 54 synthetic conditions, *Bok Choy* analysis consumed roughly 3.0 hours. Conversely, *ImageJ* would have consumed an excessive amount of time, nearly 120.8 hours for the same dataset. For a single image, *Bok Choy* completed the task of characterizing about 10 crystals in 0.18 minutes, while *ImageJ* finished in 7.25 minutes.

The efficiency benefits are not only numerical but also feature the manageable, automated nature of the *Bok Choy* workflow, which significantly cuts the demand for manual involvement. Such an advantage makes *Bok Choy* exceptionally compatible for high-throughput and all-encompassing experimental studies, where fast data analysis is imperative to draw timely conclusions.

Conclusion

Baseline vs. Best Condition

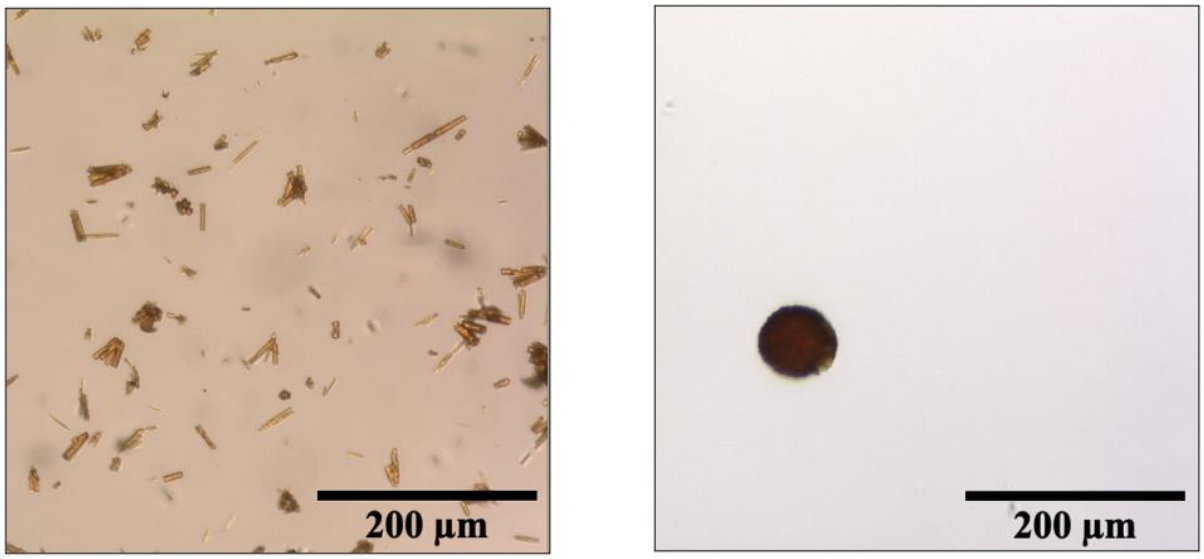

Figure 46 shows the baseline vs. the optimal AR crystals.

This comparison in Figure 46 highlights the dramatic improvement achieved by optimizing synthesis conditions. The original recipe, represented by 1I, yielded crystals with a median AR of around 5.8. These crystals exhibited a heterogeneous distribution and a lack of uniformity, which can compromise their performance in applications requiring precise crystal AR.

In contrast, the optimized 5II with buffer produced crystals with a significantly lower median AR of ~1.05, with a caveat that some may be involved with crystallization extending from the center of the entity rather than being completely spherical as can be thought of in the first glance. This represents a substantial improvement in crystals homogeneity and their AR. This observation recommends that there is often more room to explore fine-tuning the parameters and initial constituents to further enhance ARs and overall crystalline structure.

Timeline

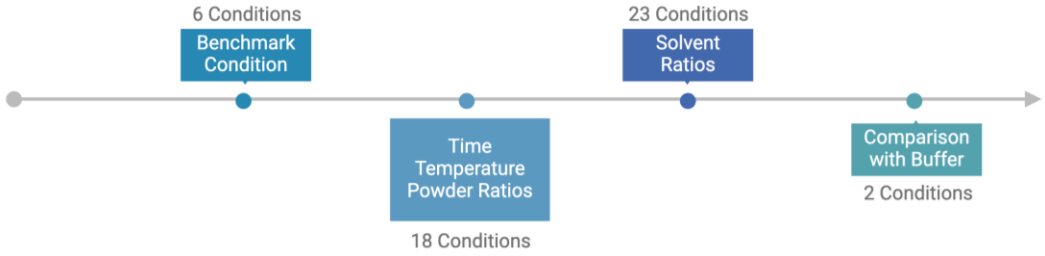

Figure 47 shows the timeline for the experiments done during this research project.

Best Conditions

Table 4 shows a comparison between baseline and optimal conditions.

Condition	Water or Buffer ul	DMF ul	Ethanol ul	Duration hr	Powder Ratio	Median AR
4II wo/ MOPS	2000	4000	4000	24	4:1	~1.48
5II w/ MOPS	1000	5000	4000	24	4:1	~1.05
1I	3333	3333	3333	24	4:1	~5.8

In conclusion, the automated approach clearly accelerated the synthesis of Co_2(dobdc) in a significant manner and helped with identifying the routes for forming the crystals with the lowest ARs. With using the automated system, the research set of experiments were not only expedited but also had greater consistency across repeated conditions. Automation synthesis was repeated twice for forms 1II to 23II, yielding reproducible results. To test the effects of different calibrations in *Mara* vs. manual pipetting, manual synthesis was repeated for conditions 8II to 13II and 18II to 23II, yielding reproducible crystals as compared in the figures in *Appendix A*.

Time and temperature experiments offered critical insights into the synthesis process, confirming the proper formation of Co_2(dobdc) congruently with theoretical expectations. These experiments explained how varying parameters influenced crystal morphology and ARs. Solvent variations also provided a broad spectrum of results, underlining the prominence of optimizing solvent volume proportions. For instance, it was observed that the absence of DMF prevented successful synthesis using the nitrate linker, emphasizing the essential role of DMF in providing the proper environment for MOF construction.

Increased ethanol volumes were associated with crystal aggregation, which negatively impacted the desired morphology and hindered estimating ARs in some occasions requiring excessive dilution post-crystallization. Conversely, lower water volumes were strongly correlated with achieving lower ARs. These findings collectively contribute to a better understanding of the factors influencing the synthesis of Co_2(dobdc) MOFs and provide a basis for enhancing future production.

Moving forward, we aim to upgrade the *Bok Choy* algorithm to make it even more vigorous and efficient, allowing faster and more accurate analysis. Moreover, we plan to incorporate a fully automated synthesis workflow with enhanced competencies, allowing for seamless operation and minimizing the need for manual intervention.

One of our key future directions is the inclusion of a newer machine learning algorithm, not yet named. This newer algorithm will exploit the current dataset to learn existing trends and predict subsequent ones, leveraging the developing database to streamline and guide the optimization process.

To further improve the synthesis process, we plan to transition from using vials to well plates made of quartz for automated synthesis. This change will enhance the consistency and scalability of the experiments, offering further acceleration of the process. These steps conjointly outline a clear trajectory for proceeding the synthesis, characterization, and application of Co_2(dobdc) MOFs.

References

"Biorender.com." BioRender. Accessed Feb 29, **2024**. https://biorender.com.

Buncel, E.; Symons, E. A. The Inherent Instability of Dimethylformamide–Water Systems Containing Hydroxide Ion. *J. Chem. Soc. D* **1970**, (0), 164–165. DOI: 10.1039/C29700000164

Carpenter, B. P.; Talosig, A. R.; Rose, B.; Di Palma, G.; Patterson, J. P. Understanding and Controlling the Nucleation and Growth of Metal–Organic Frameworks. *Chem. Soc. Rev.* **2023**, DOI: 10.1039/D3CS00312D.

Colwell, K. A.; Jackson, M. N.; Torres-Gavosto, R. M.; Jawahery, S.; Vlaisavljevich, B.; Falkowski, J. M.; Smit, B.; Weston, S. C.; Long, J. R. Buffered Coordination Modulation as a Means of Controlling Crystal Morphology and Molecular Diffusion in an Anisotropic Metal–Organic Framework. *J. Am. Chem. Soc.* **2021**, *143* (13), 5044–5052. https://doi.org/10.1021/jacs.1c00136.

Gonzalez, M. I.; Mason, J. A.; Bloch, E. D.; Teat, S. J.; Gagnon, K. J.; Morrison, G. Y.; Queen, W. L.; Long, J. R. Structural Characterization of Framework–Gas Interactions in the Metal–Organic Framework Co2(dobdc) by In Situ Single-Crystal X-ray Diffraction. *Chem. Sci.* **2017**, DOI: 10.1039/C7SC00449D.

Good, N. E.; Winget, G. D.; Winter, W.; Connolly, T. N.; Izawa, S.; Singh, R. M. M. Hydrogen Ion Buffers for Biological Research. *Biochemistry* **1966**, *5* (2), 467–477. https://doi.org/10.1021/bi00866a011

Liu, X.; Chee, S. W.; Raj, S.; Mirsaidov, U. Three-step Nucleation of Metal–Organic Framework Nanocrystals. *Proc. Natl. Acad. Sci. U.S.A.* **2021**, *118*(10), e2008880118. DOI: 10.1073/pnas.2008880118.

Marshall, C. R.; Staudhammer, S. A.; Brozek, C. K. Size Control over Metal–Organic Framework Porous Nanocrystals. Chem. Sci**.** *2019*, **10**, 9396–9408. https://doi.org/10.1039/C9SC03802G.

Parambil, J.; Heng, J. Y. Y. "Seeding in Crystallisation." In *Engineering Crystallography: From Molecule to Crystal to Functional Form*; NATO Science for Peace and Security Series A: Chemistry and Biology **2017**, pp 235-245. DOI: 10.1007/978-94-024-1117-1_13

Raptopoulou, C. P. Metal-Organic Frameworks: Synthetic Methods and Potential Applications. *Materials* **2021**, *14*(2), 310. DOI: 10.3390/ma14020310.

Sumida, K.; Rogow, D. L.; Mason, J. A.; McDonald, T. M.; Bloch, E. D.; Herm, Z. R.; Bae, T.-H.; Long, J. R. Carbon Dioxide Capture in Metal–Organic Frameworks. *Chem. Rev.* **2012**, *112* (2), 724–781. https://doi.org/10.1021/cr2003272.

Wang, J.; Imaz, I.; Maspoch, D. Metal−Organic Frameworks: Why Make Them Small? *Small Struct.* **2022**, *3* (1), 2100126. https://doi.org/10.1002/sstr.202100126.

Zhang, M.; Fu, J.; Ren, H.; Li, S.; Sun, X.; Jiao, Q. Facile Recrystallization Process for Tuning the Crystal Morphology and Thermal Safety of Industrial Grade PYX. *Molecules* **2023**, *28*(12), 4735. DOI: 10.3390/molecules28124735.

Appendix A

Bok Choy V3.0:

- Image Processing for Microscopic Images
  - Convert the image to grayscale before transforming it into an array.
  - Apply Multi-Otsu Thresholding from Scikit-Image to determine thresholds based on pixel intensity, segmenting the histogram into three distinct regions.
- Separation of Image Using Multi-Otsu Thresholding
  - The histogram is used to divide the image into three distinct regions, creating three separate images.
- Gaussian Blurring and Morphological Closing
  - Applied to reduce noise and improve image quality.
  - Optimal images were chosen based on the clarity of microscopic boundaries in the binary image.
  - Morphological Closing from OpenCV was used to close small holes within contours to improve overall image quality.
- Contour Detection and Visualization
  - Used the find_contours function from Scikit-Image to identify boundaries of enclosed regions.
  - Calculated contour areas using the Shoelace Formula.
  - Unwanted contours were filtered out by applying a minimum and maximum area threshold.
- Contour-Based RGB Value Extraction and Histogram Plotting
  - Extracted RGB values from each contour were used to analyze color distribution within the contours.
  - The extracted RGB values were plotted as a histogram to visualize their distribution and frequency.
  - A best-fitted curve was plotted over the histogram, and peak detection was applied to identify the peaks.
  - The maximum number of peaks determined the number of clusters to be used in further analysis.
- Unsupervised Learning (Clustering)
  - Calculated the mean RGB value for each contour to represent the overall color of the enclosed region.
  - Applied K-Means clustering to classify the regions based on their mean RGB values.
  - Used clustering to distinguish between microsized crystals and impurities with differing mean RGB values.
  - Selected the cluster with the highest mean RGB values and generated a binary mask for the selected cluster.
- Plotting Convex Hulls
  - All contours from the selected cluster were plotted to calculate their convexity index.
  - The convexity index is defined as:
    - Convexity Index=Original AreaConvex Hull Area

    - A convexity index threshold of **0.865** was set, based on the literature: *"A novel image analysis technique for 2D characterization of overlapping needle-like crystals."*
    - **Contours with a convexity index < 0.865**:
        - Appended to the list of red contours, representing impurities or overlapping crystals.
    - **Contours with a convexity index ≥ 0.865**:
        - Classified as single crystals.
- Plotting Detected Lines for Red Contours
    - Applied cv2.Canny edge detection to the red contour mask to identify edges.
    - Used Probabilistic Hough Line Transformation to detect line segments within the red contour mask.
    - Lines shorter than 20 pixels (calculated using the Euclidean distance formula) were removed automatically.
    - Calculated angles of the detected lines for each lines in the remaining red contour.
    - Compare angles of lines within the same contour.
    - Lines with an angular difference of less than 15 degrees (determined through trial and error) were classified into the same group.
- Best-Fit Bounding Boxes with Grouped Line
    - Applied Principal Component Analysis (PCA) to the grouped lines to determine their overall orientation and distribution.
    - Generated a best-fit bounding box for each red contour using the grouped lines' PCA results.
    - The bounding boxes were plotted to highlight the regions of interest within the red contours.
- Bounding Box Plotting for Blue Contours
    - Drew the minimum bounding rectangle for all blue contours.
    - Checked if the bounding box touched the edge of the image.
        - If a box touched the edge, it was excluded from specific calculations.
- Filtering Bounding Boxes by Area and ARs:
    - Filtered out bounding boxes with unwanted contour areas or ARs.
    - Only bounding boxes that met the specified area and AR criteria were retained.
    - Stored the ARs of the remaining bounding boxes in a list for further analysis.

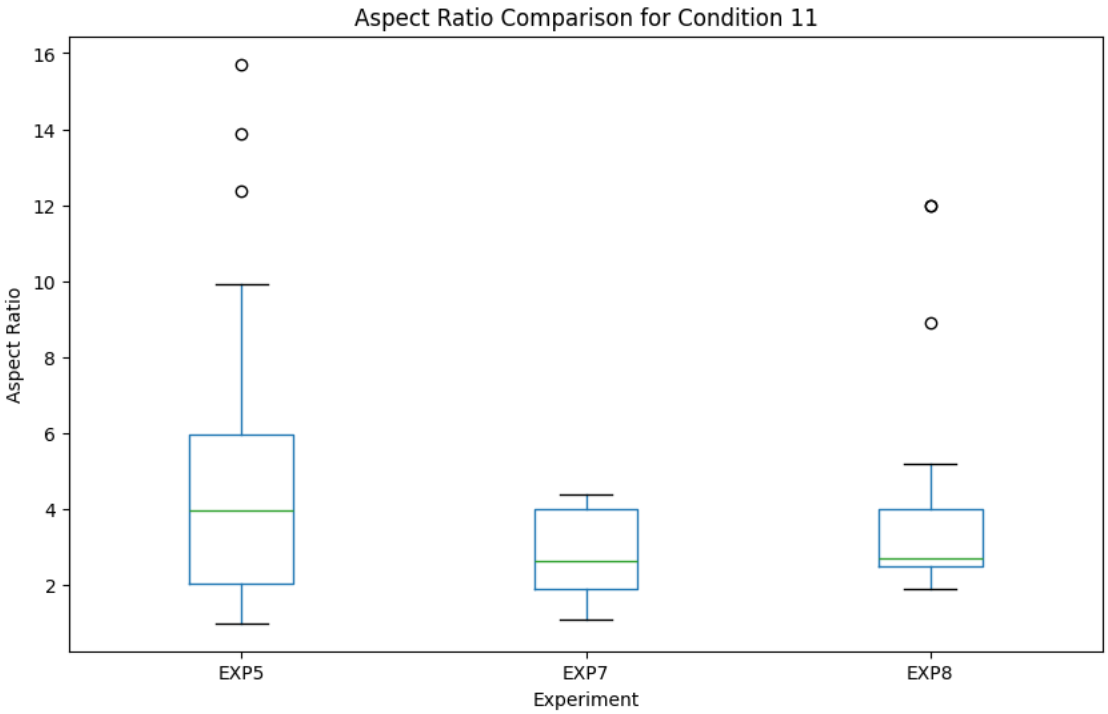

Figure 48

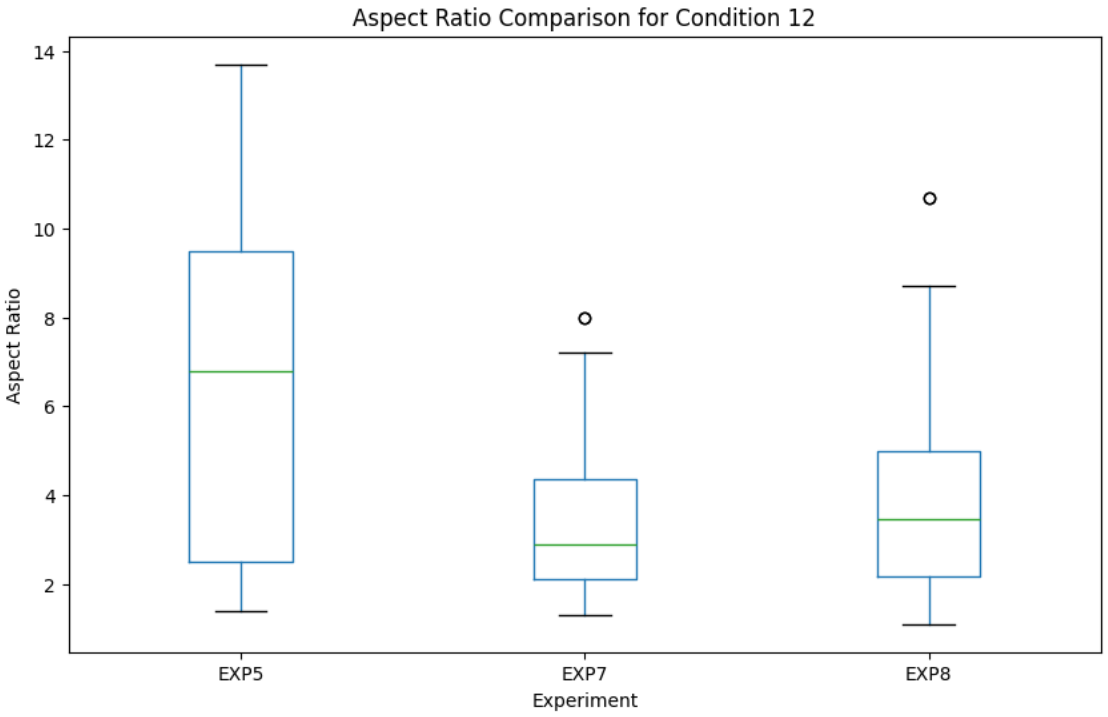

Figure 49

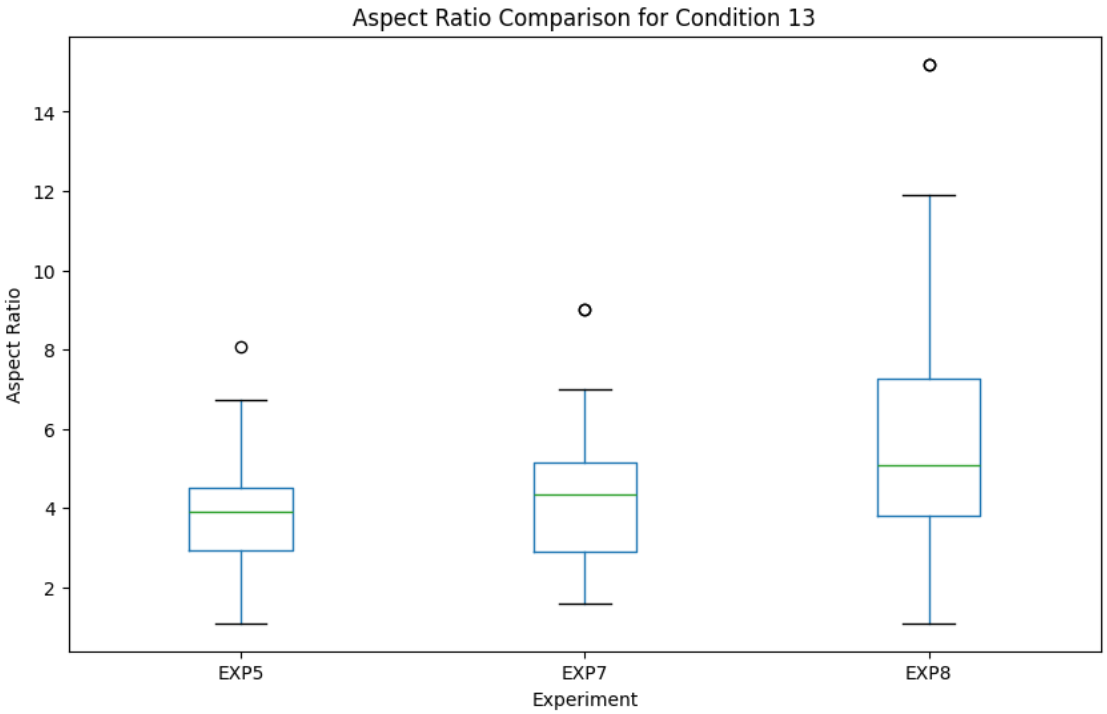

Figure 50

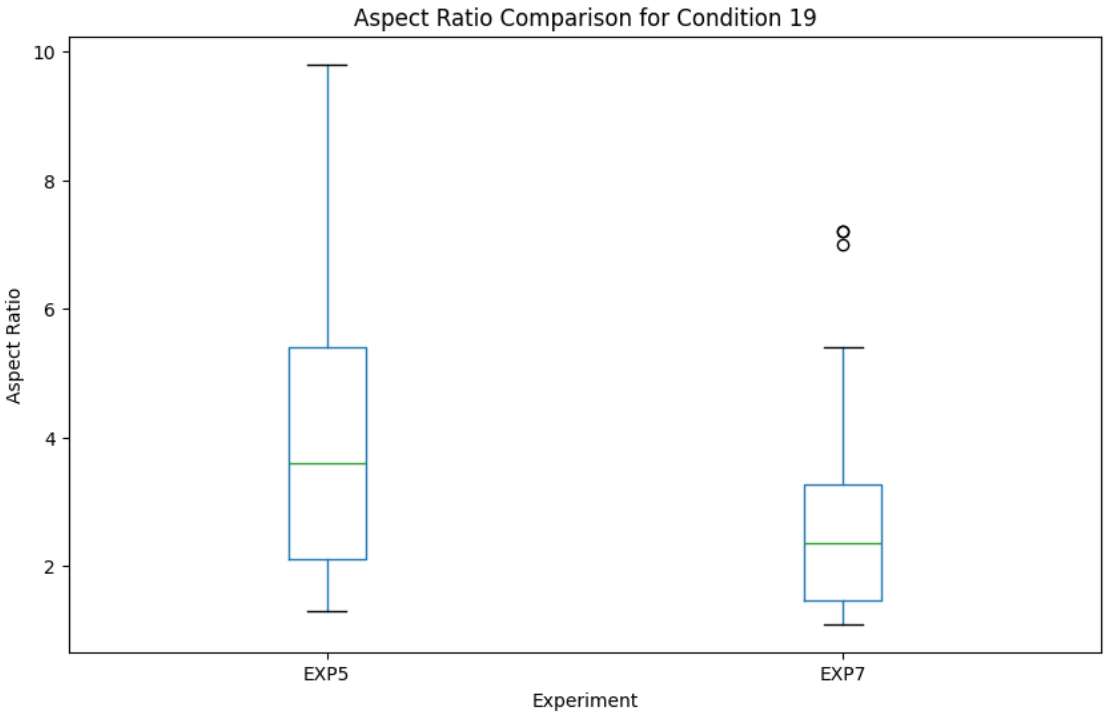

Figure 51

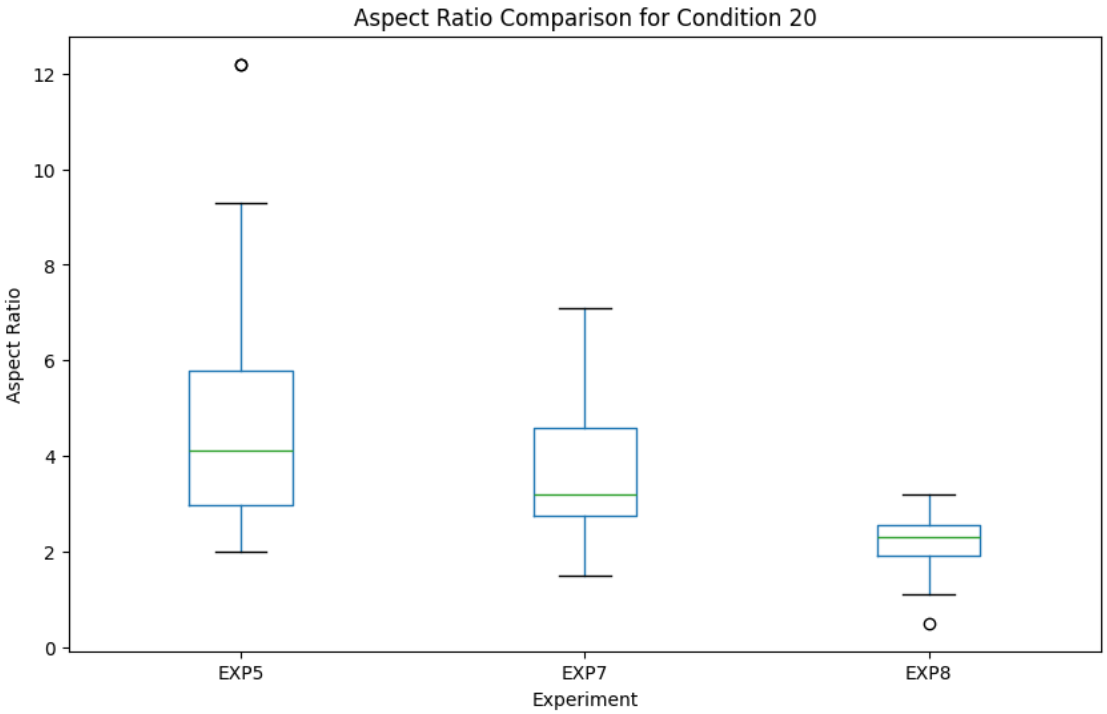

Figure 52

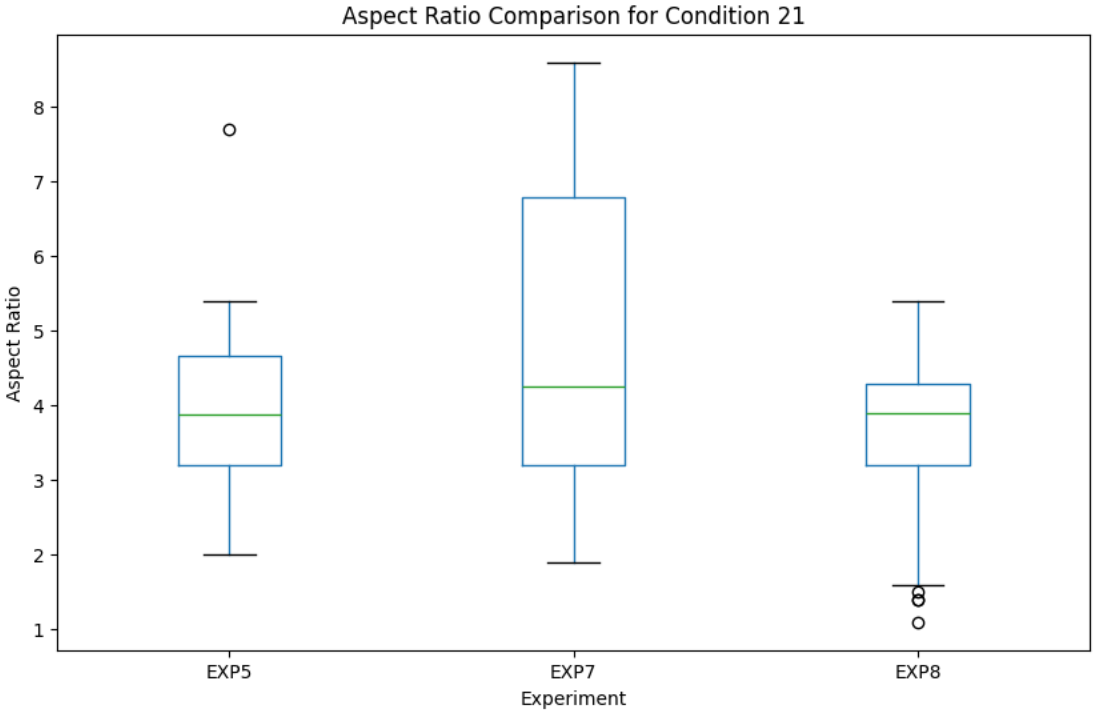

Figure 53

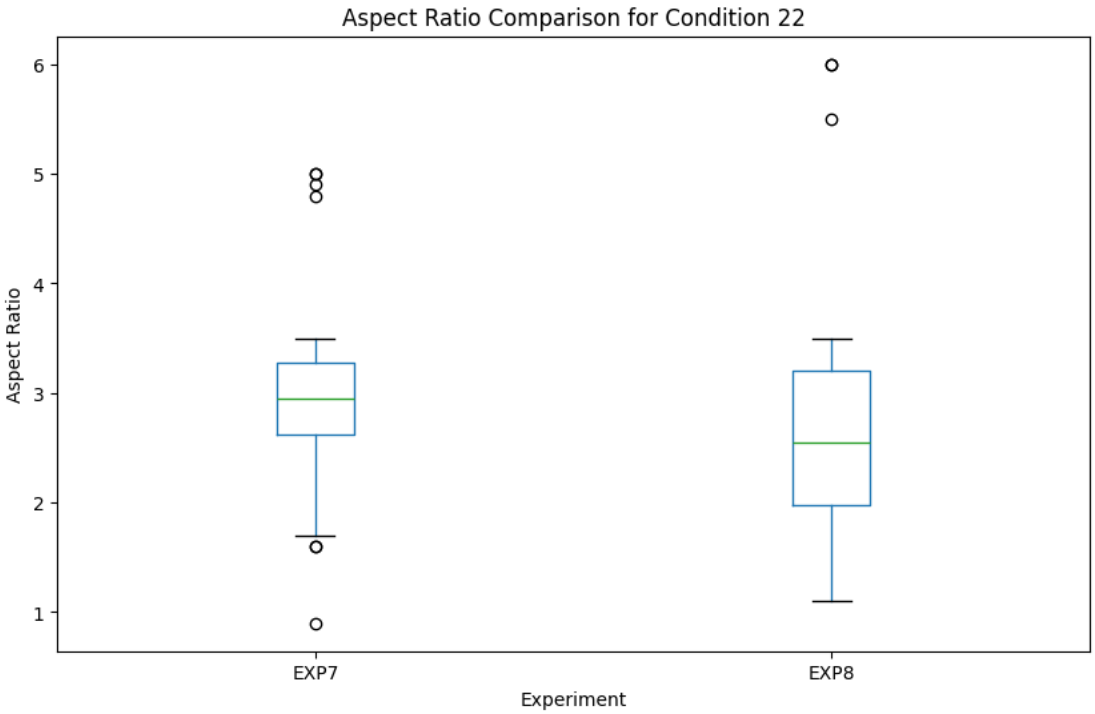

Figure 54

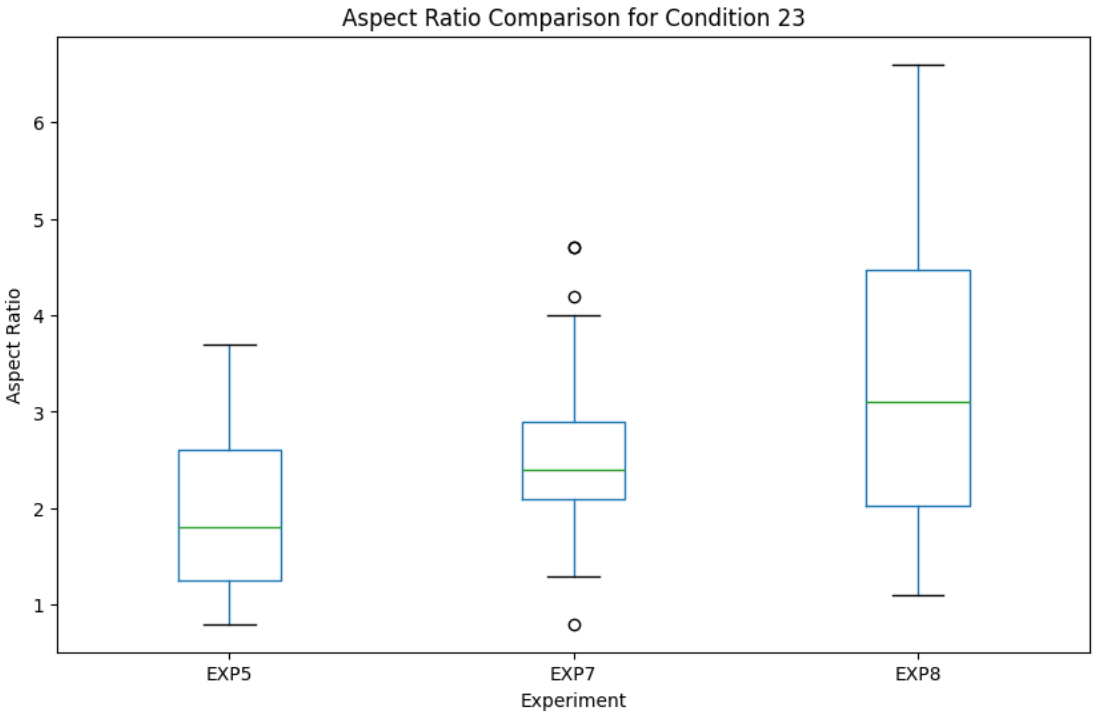

Figure 55

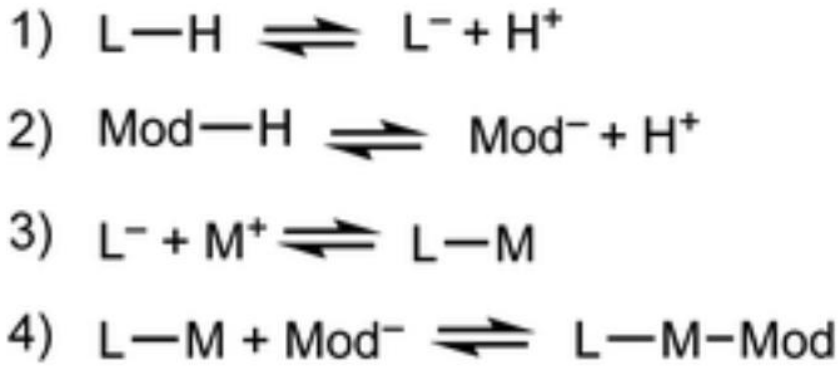

Figure 56 equation of equilibria involved in MOF synthesis as shown by Marshall et al. 2019.